Powder Technology 452 (2025) 120542

Contents lists available at ScienceDirect

Powder Technology

journal homepage: www.journals.elsevier.com/powder-technology

Evaluating cohesive models in discrete element simulation through drawdown test with new assessment perspectives

Thien Q. Huynh [a], Thanh T. Nguyen [b,*], Buddhima Indraratna [c]

[a] *PhD Candidate, Transport Research Centre, University of Technology Sydney, NSW 2007, Australia*
[b] *Senior Lecturer, DECRA/Chancellor's Fellow, Transport Research Centre, School of Civil and Environmental Engineering, University of Technology Sydney, Australia*
[c] *Distinguished Professor of Civil Engineering, Director of Transport Research Centre, University of Technology Sydney, NSW 2007, Australia*

GRAPHICAL ABSTRACT

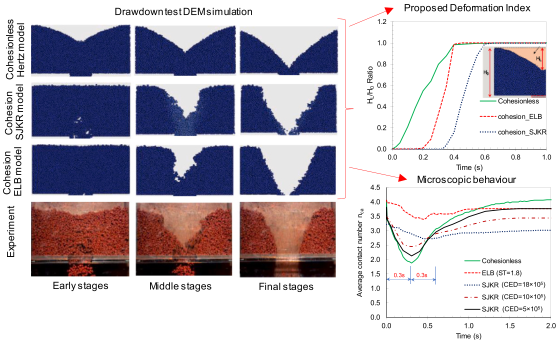

ARTICLE INFO

Keywords:
Cohesive model
Liquid-bridge model
SJKR
Porous structure
Drawdown test

ABSTRACT

This study explores the time-dependent and micro-to-macro behaviours of cohesive wet granules through discrete element simulation of a widely employed calibration procedure, i.e., drawdown test. Two distinct cohesive models, i.e., the Easo Liquid-Bridge (ELB) and simplified JKR (SJKR) are adopted. Their simulation results are not only validated with past experimental observations, but also compared with each other in multiple aspects. The results show substantial difference in time-dependent deformation and mass-volume change correlations characterised by the ELB and SJKR models, though they both show good agreement in bulk parameters with the experiment at final stage of drawdown test. Moreover, this study points out critical deviations in microscale features such as the contact network and porous structure that determines the macroscale responses under different concepts of cohesive contact. The results suggest new assessment parameters for modelling cohesive material and provide a deeper insight into the micro-to-macro understanding.

1. Introduction

Understanding microscopic interactions between constituent particles of materials such as soil, rock and powder is crucial to explain their macroscopic behaviour. The interaction between particles is often described by their frictional and cohesive contacts, with the latter

---

* Corresponding author.
E-mail address: thanh.nguyen-4@uts.edu.au (T.T. Nguyen).

https://doi.org/10.1016/j.powtec.2024.120542
Received 28 June 2024; Received in revised form 13 October 2024; Accepted 7 December 2024
Available online 13 December 2024

arising from molecular attractions between contacting surfaces such as the van der Waals forces between fine particles, capillary forces in wet particles, and electrostatic forces [1–4]. While frictional resistance can be determined based on the shape and surface features of particles [5,6], it is often more challenging to capture the interparticle cohesive forces accurately due to their complex nature [7,8]. Cohesive forces can vary widely, depending on many factors such as the surface roughness, relative displacement, chemical features, and environmental conditions [5,7,9]. This is why there are so many theoretical studies to characterize the behaviour of interparticle cohesion and its influence on the macroscale response of materials [10,11]. Of these, the discrete element method (DEM), which can model the particulate behaviour of materials in greater detail, has proven to be an effective and reliable approach [12–14]. However, because the behaviour of interparticle cohesive contacts is very complex, most DEM studies face considerable limitations in modelling cohesive materials such as the simplified breakage mechanism of cohesive bonds [15,16], the linearisation of force-displacement relationship [16,17], the neglected time-dependent response [18,19], and the narrow range of particle sizes [20,21], among others. This has posed significant challenges to modelling and thus the critical demand for a complete and more rigorous model that will enable DEM simulations to capture the true behaviour of cohesive materials.

One of the most important steps in DEM simulation is the selection of model parameters. Fundamental experiments such as rotating drum, slump, lifting cylinder or funnel, drawdown and direct shear tests are normally used for calibration [6,19,20,22,23], whereas more complex experiments such as the dynamic impact and fume tests are used to simulate the flow behaviour of cohesive materials [7,14,24]. Despite this diversity in experimental approaches, previous studies often focused on a single aspect of calibration tests [18,20,22], leading to incomplete or biased considerations of material responses. For example, using the angle of repose (AoR) as a single macro-parameter to calibrate a DEM model does not always reflect the intrinsic mechanism of cohesive contact very well. The curve fitting between experimental and numerical data is manipulated through a tuning process of multiple parameters. By assessing different calibration tests, Roessler et al. [20] showed that calibrating the DEM parameters based solely on single-parameter test results is generally not feasible.

Of various calibration tests, the drawdown (DD) test, where multiple parameters can be used for calibration has become a reliable and effective selection. It is noteworthy that the term “drawdown” (or draw-down in some studies) implies a reduction (loss) process that has been used widely in different fields such as pressure and water drawdown tests in hydrology. In granular research, DD test often refers to a process that granular material flows out from the upper to lower boxes, thus the loss of mass in the upper region. The DD test simultaneously offers 4 different criteria within a single test, i.e., the angle of repose (AoR) observed in the lower box, the shear angle (SA) measured in the upper box, the flow time, and the mass loss. Although these 4 parameters can be used to represent different aspects of DD test outcomes, concurrent changes in the volume and mass of material during particle flow are not quantitatively incorporated into these 4 parameters, so the characterisation of this test is incomplete. In fact, these parameters are only determined at the end of the test (final stage), so their time-dependent behaviour is often not attended properly. Moreover, despite the abundance of research on DD tests [14,18–20,25], there remain considerable gaps in understanding the underlying mechanisms and microscale evolution that govern the test outcomes. In fact, previous studies [14,18] mainly focused on external manifestations such as the AoR and the shear angle, while neglecting the transformation of those internal structures and contact features which actually drive the external responses. Furthermore, the linkage between micro-parameters (e.g., the interparticle forces and contact developments) and macro-features (e.g., the shear angle and AoR) was not addressed in previous DD test modelling [14,18,20]. This makes the practical implications of interparticle cohesion very limited.

There are different cohesive contact models that have been used to simulate wet granules in previous studies [14,19]. However, the question of which model can accurately describe the nature of cohesive contacts has not been clarified. For instance, the Johnson Kendall-Roberts (JKR) model and its simplified version (SJKR) have become one of the most popular choices for simulating wet granular materials. Many previous applications [19,25,26] often varied the model parameters to achieve the best outcomes, but they relied heavily on macro-scale observations (bulk assessment) rather than a thorough micro-to-macro approach. A good agreement of geometric features such as the slope angle does not always mean a reasonable prediction of the porous characteristics of the material. This is because the JKR model was originally developed for soft particles with deformable contact where particle attraction is mainly driven by electrostatic forces. Its relevance to model wet materials hence requires an urgent reassessment.

In view of the above, this current study aims to improve DEM simulation of DD test by developing a thorough assessment on the time-dependent and micro-to-macro behaviour of cohesive materials. The discrete element method (DEM) is employed as the fundamental platform, while the Easo Liquid Bridge (ELB) model is used to simulate wet granular material in tandem with the SJKR model. The numerical results are validated with experimental data from past studies, meanwhile extensive numerical investigations are carried out to explore and evaluate multiple aspects of the 2 models. This study proposes new parameters incorporating time-dependent deformation (i.e., the deformation index DI) and correlation between the volumetric and mass variations of material during simulation of DD test. Besides macroscale aspect, a microscale analysis reveals that different modelling concepts of interparticle cohesion can lead to notable variations in the particulate contact network and the corresponding porous structure. This study also reveals novel findings on the intrinsic relationships between the micro- and macro-quantities of wet materials, and provide valuable implications to the modelling of cohesive granules in DEM.

2. Theoretical background

2.1. DEM and Hertz contact model

This current study utilizes the discrete element method (DEM) which is based on the fundamental theories of Newton’s Laws incorporated in LIGGGHTS [27]; while these theories and governing equations are not reiterated in this paper, they can be found in previous studies [8,28,29]. When non-cohesive granular materials are considered in DEM, the Hertz-Mindlin (Hertz) contact model is normally preferred [20,30,31] because it depicts a non-linear relationship between the contact force (i.e., the normal force $F^{ij}_{n,H}$ and the shear force $F^{ij}_{s,H}$) and the overlap (i.e., normal overlap δ_n and the shear overlap δ_s) between two particles where the normal and shear (tangential) contact stiffnesses $k_n$and k_s are described in Eq. (1) and (2), respectively. It is noteworthy that the original Hertz model does not consider cohesion and friction of contact between particles, meanwhile other contact components such as the tangential (sliding) friction (i.e., Coulomb friction limit, $\mu F^{ij}_{n,H}$ described in Eq.(2)) and damping effects (i.e., the damping in normal direction F^d_n and shear direction F^d_s shown in Eq.(3) and (4)) are computed independently in DEM [32,33]. The total contact force can then be obtained by combining all different components that are considered in a DEM simulation. To distinguish the contact force by Hertz from other factors, the subscript H is used, i.e.,

$$F^{ij}_{n,H} = \left(\frac{4}{3}E^* \sqrt{R^* \delta_n}\right)\delta_n = k_n \delta_n \tag{1}$$

$$F^{ij}_{s,H} = \left(8G^* \sqrt{R^* \delta_n}\right)\delta_s = k_s \delta_s \leq \mu F^{ij}_{n,H} \tag{2}$$

$$F_n^d = -2\beta_n\sqrt{m^*\frac{3}{2}k_n}\dot{\delta}_n \tag{3}$$

$$F_s^d = -2\beta_s\dot{\delta}_s \tag{4}$$

where m^*, E^*, G^*, and $R^*$are the effective mass, Young's modulus, shear modulus, and the effective radius of two spherical particles, as determined from the Young's modulus (E_1, E_2), Poisson ratios (υ_1, ν_2), and radius (R_1, R_2) of two contact particles; meanwhile δ_n and δ_s are the normal and shear (tangential) overlap between particles, respectively; μ is the friction coefficient; β_n and β_s are the normal and shear critical damping ratio, $\dot{\delta_n}$ and $\dot{\delta_s}$ are the relative normal and shear translational velocity.

2.2. JKR and its simplified model

In order to consider the influence of cohesion on contact behaviour, Johnson et al. [11] included the tensile force components induced by cohesion into the Hertz contact theory (compression force), this resulted in the so-called Johnson-Kendell-Roberts (JKR) model. This model accounts for the collective action of all the cohesive forces (i.e., the van der Waals, electrostatic, and capillary forces) by the notion of attractive surface energy. The JKR model has been used extensively across different disciplines to model various materials such as fines, wet course particles and soft cohesive particles [34,35]. The relationship in the JKR model between the normal contact forces $F^{ij}_{n,J}$ and the enlarged contact radius a depends on the attractive surface energies of contact γ^*, which is governed by Eq. (5) and (6) [11].

$$F_{n,J} = \frac{4E^*a^3}{3R^*} - \sqrt{8\pi\gamma^*E^*a^3} \tag{5}$$

$$\delta_n = \frac{a^2}{R^*} - \left(\frac{2\pi\gamma^*a}{E^*}\right)^{1/2} \tag{6}$$

where $\gamma^*$is the attractive surface energy of contact between particles i and j. Note here that unlike Hertz theory, the normal overlap δ_n is a function of the contact radius a and the surface energy term γ^*.

In DEM, a close-form solution for the full JKR model is almost impossible to compute due to the 4th order quadratic equation of the contact feature described in Eq. (6), thus numerical procedures such as Parteli et al. [34] have been used. Since existing numerical solutions for Eq. (6) usually require many parameters, and thus a low efficiency of computation, several simplifications in determining the contact radius and cohesive force components have been applied. This can be seen through the simplified JKR models (SJKR) where the contact force incorporating attraction between two particles is governed by Eq. (7) as follows.

$$F^{ij}_{n,S} = \left(\frac{4}{3}E^*\sqrt{R^*\delta_n}\right)\delta_n - A\times CED = k_n\delta_n - A\times CED \tag{7}$$

In this method the SJKR model assumes that the contact radius is calculated directly from the effective radius and the normal overlap of two contact particles (i.e., $a = \sqrt{R^*\delta_n}$). Furthermore, this model has introduced a new cohesion term called the cohesive energy density (CED) (J/m^3), it is defined as the volumetric energy required to detach a particle from its contacting neighbour [36]; the cohesive force is thus a product of CED (J/m^3) and the contact area A (i.e., $A = \pi a^2$). This also means that the CED term yielded from this simplification process has in fact deviated significantly from the nature of cohesive energy in the original JKR model. Despite this complexity, SJKR has been widely used in various contexts such as wet sands, mining particles and powders [8,14,19]. It is thus addressed in our study.

2.3. Liquid-bridge model

The capillary and viscous forces generated by pore fluid (e.g., pore water in soil) make cohesive bonds between particles; this phenomenon can be captured via the so-called liquid-bridge theories [10,37–39]. In particular, the attractive force induced by the liquid surface film on particles is added to Hertz contact theory Eq. (8) to form a liquid-bridge model which includes the rupture distance ($D_{rupture}$) and force (F_L) (i.e., capillary force and viscous force). The rupture distance depends on the surface liquid bridge volume (V_{LB}) which occurs upon contact and is represented by Eq. (9). For the current DEM simulations, the calculation of capillary force, i.e., Eq. (10) proposed by Easo et al. [40] and referred to as the Easo liquid-bridge (ELB) model, was adopted. This model leverages various previous liquid bridge models [2,38,41], where the rupture force reaches its peak at zero normal overlap (δ_n).

$$F^{ij}_{n,E} = \left(\frac{4}{3}E^*\sqrt{R^*\delta_n}\right)\delta_n - F_L = k_n\delta_n - F_L \tag{8}$$

$$D_{rupture} = (1+0.5\theta)V_{LB}^{1/3} \tag{9}$$

where θ is the average contact angle between two particles i, j and liquid: $\theta = 0.5(\theta_i + \theta_j)$

$$F_L = \pi ST\sqrt{R_1R_2}\left[C + exp\left(A\frac{D}{R_2} + B\right)\right] \tag{10}$$

where ST is the liquid surface tension and D denotes the distance between the surfaces of two particles. The factors *A, B and C* are determined from the surface liquid bridge volume (V_{LB}), the average particle-liquid contact angle of two particles (θ), and the radius of the bigger particle (i.e., R_2) according to Eq. (11)–(13). These factors can be determined from experimental processes, for example, previous studies [2,38,42] have shown that the contact angle has a trivial impact on the profile of wet material and its reasonable values from experimental observation are between 30^0 and 50^0. The precise calculation of the V_{LB} from a capillary grain-pair experiment can be found in previous studies [2,10].

$$A = -1.1\left(\frac{V_{LB}}{R_2^3}\right)^{-0.53} \tag{11}$$

$$B = \left(-0.148ln\left(\frac{V_{LB}}{R_2^3}\right) - 0.96\right)\theta^2 - 0.0082ln\left(\frac{V_{LB}}{R_2^3}\right) + 0.48 \tag{12}$$

$$C = 0.0018ln\left(\frac{V_{LB}}{R_2^3}\right) + 0.078 \tag{13}$$

2.4. Conceptual differences between SJKR and ELB

Fig. 1 demonstrates different stages of contact between two particles according to the ELB and SJKR models. When two particles penetrate each other, the overlap and contact radius (a) are formed. With the SJKR model, the contact force, including tangential and normal components, are only derived from the internal contact area so when the overlap is equal to zero the contact force vanishes, and a rupture of contact occurs (see Fig. 1a). On the other hand, the ELB model considers the influence of liquid on the contact behaviour so when the two particles begin to separate from each other (i.e., $\delta_n = 0, a = 0$), the contact (attractive) force remains and is equal to the tensile force of the liquid bridge. The attractive force becomes zero when the liquid bridge breaks (Fig. 1b). It is noteworthy that when the overlap is positive, the normal and tangential forces interact each other through the normal overlap δ_n as the mutual governing factor (see Eq.(1) to (4)). However, when the overlap becomes negative, only the attractive (normal) force is considered.

Fig. 2 depicts the pathway (relationship between the interactive

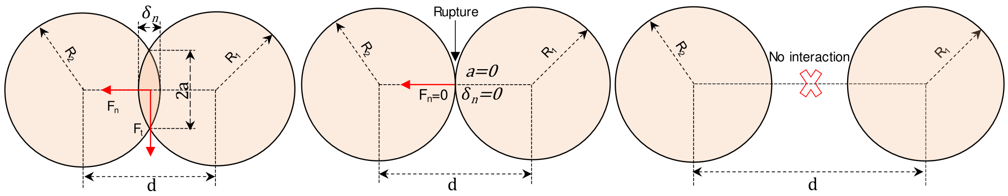

(a) SJKR model

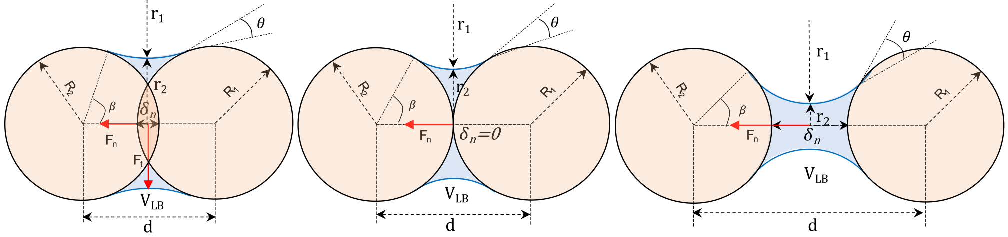

(b) ELB model

Fig. 1. Development of contact between two particles described by (a) the SJKR model and (b) the ELB model.

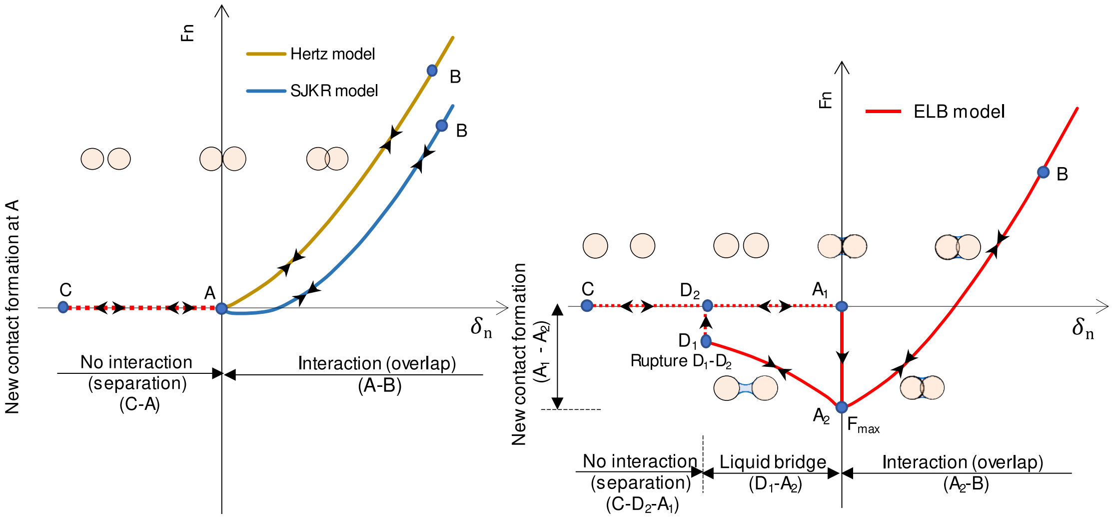

(a) (b)

Fig. 2. Development of contact force with relative displacement between two particles in contact: (a) the non-cohesive Hertz and cohesive SJKR models, and (b) the cohesive ELB model.

force and relative displacement) of contact formation and rupture between two particles. The Hertz and SJKR models have similar pathways (Fig. 2a), where the contact force is only generated and develops when two particles begin to touch (i.e., Point A) and penetrate each other. Unlike the Hertz model, the introduction of cohesion in SJKR reduces the compressive part of the total contact force, given the same degree of overlap between particles. The tensile force (negative contact force) exists predominantly at early stage of the contact (small δ_n) before changing to the fully compressive stage when δ_n increases. For the ELB model, a new contact is only formed when two particles meet each other at Point A_1 (see Fig. 2b), which immediately produces the attractive force F_{max} at Point A_2. In the path A_2-B two particles penetrate each other, whereas they separate from each other in path A_2-D_1-D_2. It is noteworthy that contact still exists at Point A_2, it only breaks at the rupture distance (Point D_1 to D_2).

The above differences in mechanism between the ELB and SJKR models indicate that the ELB would become more relevant to simulate wet materials such as sands and mining granules. The cohesion induced by capillary and liquid tension between particles is represented through the development and breakage of liquid bridge, as depicted in Fig. 1, Fig. 2 and Eq. (8) to Eq. (13) above. On the other hand, the SJKR, despite simplicity, can be used as a general form combining different types of attractive forces such as the Van der Waals, electrostatic and liquid tension, which is why it has been used widely in various contexts such as wet sand [19,23,43], iron ore fines [14], bauxite particles [18], biomass powder [44], and so on.

2.5. Rolling friction

This current study considered the influence of particle shape on rolling behaviour through the rolling resistance. Iwashita and Oda [45] suggested that the maximum rolling resistance torque (M_r^{max}) can be computed with respect to the rolling friction coefficient (μ_r), while Ai et al. [46] used the elastic-spring-dashpot (EPSD2) to simulate rolling resistance between two particles. This model introduces an extra torque that counteracts the rotational motion of the particles at their contact points, as described by Eq. (14). The EPSD2 model can be modified to accommodate a higher value of rolling stiffness that can overcome the oscillatory behaviour and eliminate the need for considering rolling damping [6].

$$M_r = -k_r \Delta\theta_r, M_r \le M_r^{max} = \mu_r R^* F_n^{ij} \tag{14}$$

where M_r and $k_r = k_t R^{*2}$ are the resistive torque and rolling stiffness, respectively; $\Delta\theta_r$ denotes the increment of relative rotation between two particles, and μ_r represents the friction coefficient of rolling resistance.

3. Drawdown test and DEM simulation

Of the different calibration tests, the drawdown (DD) test is the preferred option because it can provide multiple aspects for determining the DEM modelling parameters; it was therefore selected for assessing the performance of the cohesive SJKR and ELB models in this study. The experimental setup for this test can be referred to previous studies [20,25]. Fig. 3 shows the key dimensions and parameters of a typical DD test apparatus. Basically, there is an upper and lower box that is connected via an opening whose size can be altered to achieve reasonable outcomes (Fig. 3a). First, the test material is placed inside the upper box and then the discharge gate is quickly opened to allow the fill material to flow into the lower box. The lower box contains the discharge material which forms a pile with a slope angle φ_r, i.e., the angle of repose (AoR). Meanwhile, the remaining material in the upper box creates two other slopes which represent the shear angle (SA), i.e., the continuous and dotted lines for cohesive and non-cohesive materials, respectively as shown in Fig. 3b. This test also determines the loss of mass by weighing the upper box and flow times of discharged material. In short, this test will enable 4 independent parameters to be obtained, i.e., (*i*) the angle of repose of the material in the lower box, (*ii*) the shear angle of remaining material in the upper box, (*iii*) the mass loss of material in the upper box, and (*iv*) the flow time of discharged material.

In this current study, the DD test conducted by Grima [18] was used to develop and validate the DEM models. In this experiment, the upper box was evenly filled with particles of wet bauxite with a 16 % moisture content. The particle size of the tested materials ranges from 4.0 mm to 9.0 mm. During and after the test, a camera was used to record any changes in shape and flow time; this resulted in the cumulative mass and angle of response in the lower box and the shear angle in the upper box estimated via image processing. The experimental results are summarized and compared with the DEM results in the next section.

In DEM simulation, the computational cost can be highly excessive, especially when the number of particles required to replicate a full-scale experiment was very large and the total number of test cases could exceed 66 as experienced in the current study. Therefore, the technique of up scaling those particles that would not significantly affect the model outcomes was used in order to reduce the computational cost [47,48]. This technique enabled the number of particles needed to fill the required volume in the upper box to decrease to 27,000 by scaling 1.5 times particle size, which significantly enhanced computational efficiency. This system included 2 boxes and an opening (see Fig. 3). The depth of upper box and lower box were 100 mm and 180 mm, respectively. Particles were then generated in the upper box but without compaction with height of 250 mm, thus mimicking real state of the material used in the experiment by Grima [18]. The opening was then activated to allow particles to travel from the upper box to the lower box. Since the particles dropped under the effect of gravity, they lost their boundary confinement and particle contacts as they moved out of the upper box. The DEM simulation was only completed when the kinetic energy of the entire system became stable at a minimal value.

Determining initial input parameters such as the friction coefficients for DEM simulations is usually a controversial and demanding process. This is why many studies adopt values directly from relevant literature [13,30], while others implement extensive calibration processes [14,19,20], depending on the research objectives. In this current

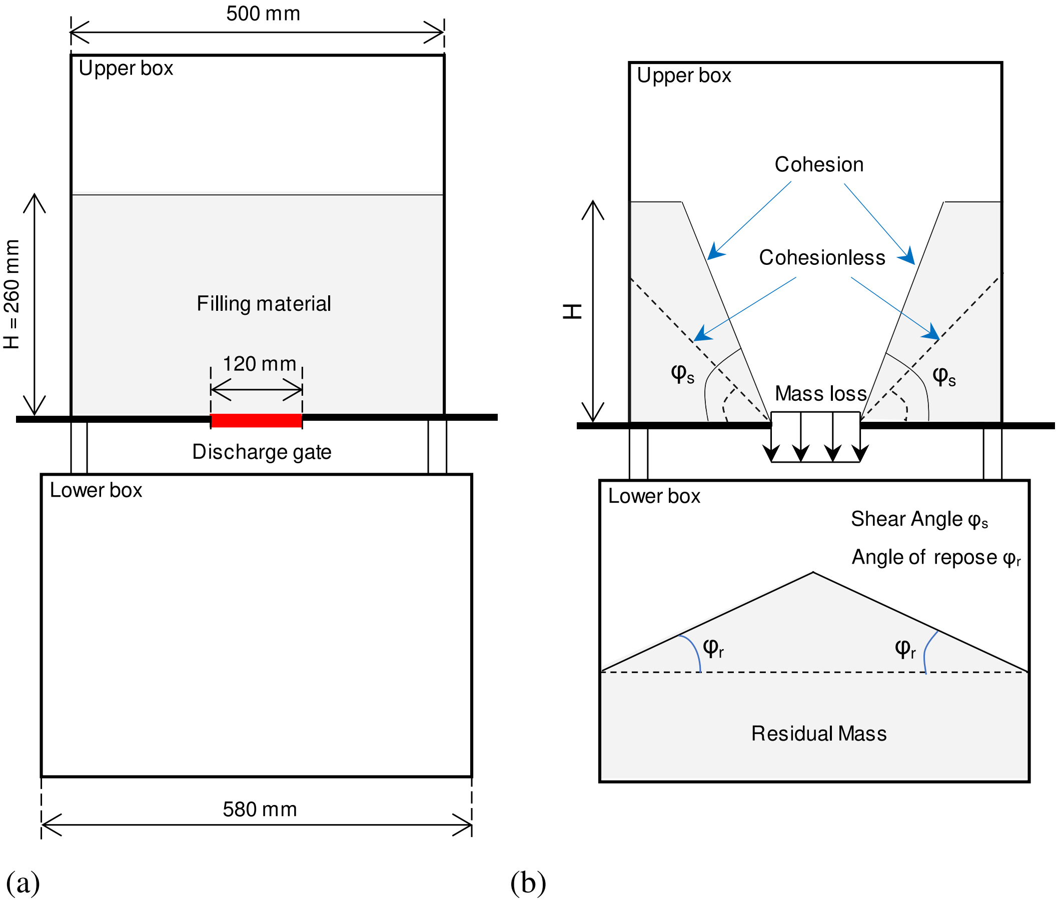

Fig. 3. Schematic of drawdown test apparatus: (a) the initial stage and (b) the final stage.

analysis, the sliding friction coefficient often varies in a narrow range and has less impact on the particle falling behaviour of granular materials remained unchanged at 0.5 for interparticle contacts and 0.35 for particle-wall contacts, with reference to previous findings [13,20]. In the meantime, the cohesion and rolling friction coefficients were varied to obtain the best prediction outcomes with respect to the experimental results. Specifically, the rolling friction coefficient was varied from 0.1 to 0.3, which is the common range for granular particles identified in literature [12,18,30,36,49].

On the other hand, the value of Cohesion Energy Density (CED) can change significantly depending on the type of materials. Grima [18] suggested CED = 35×10^5 (J/m^3) for highly cohesive materials (i.e., wet washed coal), while others used CED in the range 6.5×10^5 - 7.5×10^5 (J/m^3) for sand with 10 % moisture content [19]. Based on experimental measurements and theoretical consideration, Carr et al. [14] proposed a range of CED for iron ore from 4×10^5 to 15×10^5 (J/m^3). Given this wide range of CED, this current study used a CED from 0 to 20×10^5 (J/m^3) with the value increment of 5×10^5 (J/m^3). For the liquid bridge model ELB, the surface tension (ST) (N/m) can also change extensively depending on the type of material, the liquid content, and the properties. Carr et al. [14] used an ST value from 1 to 3.5 (N/m) for iron ore fines with 18.5 % moisture content in the shear box and dynamic cohesion impact tests. The range of ST values in this current study are from 0 to 2 (N/m) with an increment of 0.3–0.5 (N/m). These DEM input parameters are summarized in Table 1.

4. DEM results and validation with experimental observation: conventional approach

A series of DEM models with the variation of cohesive coefficients (i.e., the CED for SJKR and ST for ELB) were carried out, and the model outcomes were compared with the experimental data to select the best sets of input parameters. Fig. 4 shows the key outcomes, i.e., the AoR and SA obtained from DEM simulations, while Fig. 5 shows the major stages of DD tests in the experiment and numerical modelling. For the SJKR model, rising cohesion and rolling resistance makes the AoR and SA increase constantly; in contrast for the ELB model, the SA increases continuously, whereas the AoR rises in the initial period and then decreases to a stable level. When the surface tension was very high at 2.0 N/m, an arch formed at the opening because the very high attractive forces between particles t prevented them from falling under gravity. With the SJKR model, when the CED reached a very large degree such as 20×10^5 J/m^3, the particle system became unstable due to the very high and unrealistic attraction between particles; they were therefore not considered in this study.

By comparing geometric features such as the AoR, SA, and flow rate (Fig. 5) between the numerical and experimental results, the best sets of model parameters were determined to be CED $=18 \times 10^5$ J/m^3, $\mu_r = 0.2$ and ST $= 1.8$ N/m, and $\mu_r = 0.2$ for the SJKR and ELB, respectively. Figure Fig. 5 shows the best results recorded over time from the DEM simulation compared to the experimental data. These results indicate that the mass loss and consequent formation of a shear angle in the upper box match the experimental outcomes quite well. The three key distinct stages at 0.2 s, 0.6 s, and 1.2 s were identified based on experimental observation and then used to assess the numerical performance.

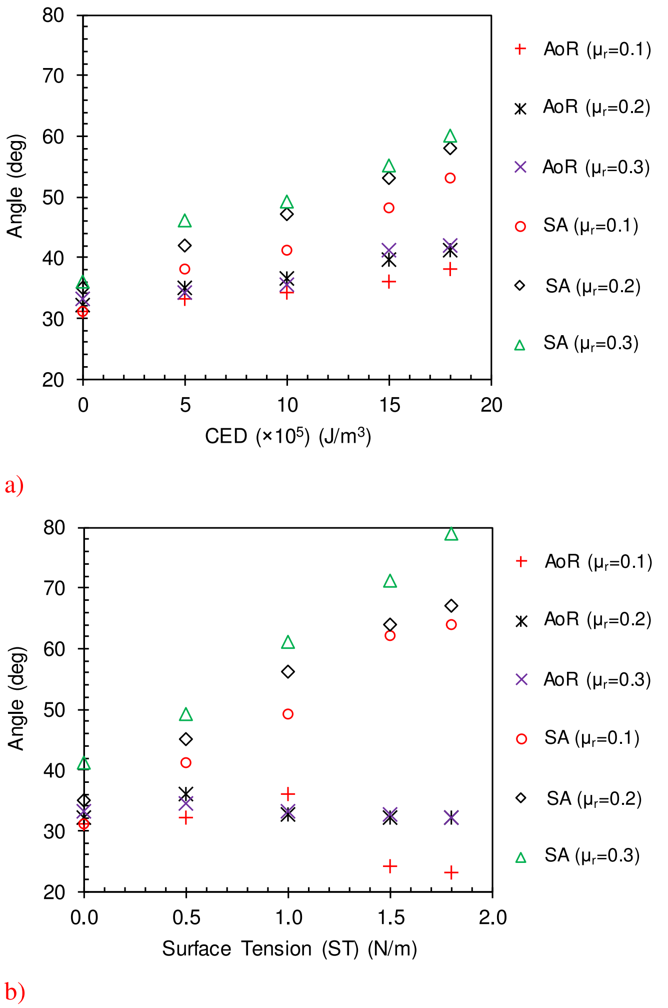

Fig. 4. The AoR and SA results from DEM with varying cohesion and rolling friction coefficients: (a) SJKR model and (b) ELB model.

Table 1
Input parameters in DEM simulation.

Parameters	Values	References
Particle density (kg/m^3)	2750	Grami [18]
Poisson's ratio	0.3	
Young modulus (Pa)	3×10^8	
Restitution coefficient	0.2	Behjani et al. [50]
Sliding friction coefficient for particle–particle/wall-particle contacts	0.5/0.35	Nguyen and Indraratna [13]
Rolling friction coefficient (μ_r)	0.1–0.3 $\Delta = 0.1$	Grami [18]; Derakhshani et al. [12]; Phan et al. [30]
Timestep (s)	10^{-5}	10 % Rayleigh time step
Cohesion Energy Density (CED) (J/m^3)	0:20 $\times 10^5$ ($\Delta = 3$–5×10^5)	Grima [18]; Ajmal et al. [19]
Surface Tension (ST) (N/m)	0:2 ($\Delta =$ 0.3–0.5)	Carr et al. [14]

Note: Δ is the value increment.

(i) *First Stage (0.2 s)*: particles began to discharge from the upper box and the top surface of the bulk material became slightly deformed at the centre. Both the SJKR and ELB models did not capture this phenomenon very well as there are clear differences in the surface displacement between the simulated and experimental results.

(ii) *Second Stage (0.6 s)*: the loss of particles at the upper box became significant and formed clear slopes on both sides of the box. The ELB model captured this stage perfectly, whereas the SJKR induced a lower amount of particle loss.

(iii) *Final (stable) Stage (1.2 s)*: all particles reached a stable state without any movement. The above results verified that the ELB model could produce much better outcomes. The shape of the material and the time to reach stable stage predicted by ELB model matched the experimental data very well. At the same time, however, the particles produced by the SJKR model were

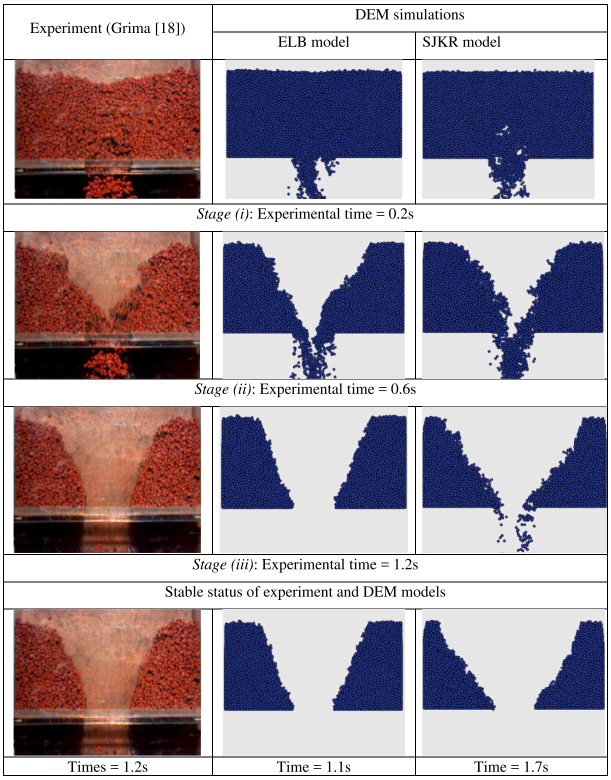

Fig. 5. Observation of experiment and DEM simulations at the best predictions: ST = 1.8 N/m for ELB model, and CED = 18 × 10^5 J/m^3 for SJKR model).

still active and only became stable after 1.7 s, which was much longer than the experiment. While previous studies [14,19,20,25] demonstrated that SJKR could reproduce the final shape of wet material in the DD test, no study considered the variations in time that needed to fully discharge and stabilise the particles.

A detailed comparison for 4 key test criteria, i.e., the AoR, SA, flow time, and mass between the experiment and numerical models is given in Table 2. It shows that the ELB model outperformed in predicting shear angle with only a 1.5 % difference between the experimental data, whereas the SJKR model resulted in 12.1 % difference. The ELB model also predicted the flow time and mass loss with only 8.3 % and 5.3 % deviations from the experimental records. These figures were much smaller than those obtained from the SJKR model. The error of AoR prediction by the ELB model was 13.2 %, which was the only aspect that came behind the SJKR model. Overall, the average deviation between the experiment and the ELB prediction was 7 %, which was much lower than that (19.9 %) induced by the SJKR, thereby attesting to the outstanding performance of ELB compared to its counterpart. Despite the large values, these 4 parameters do not reflect the time-dependent variation in the shape of the material, especially in the upper box. For example, Fig. 5 shows that the change of shape in the experiment did not match the model results very well during the 1st Stage but it improved substantially in the 2nd Stage. This means that a more comprehensive criterion that can represent the model performance over time and at different stages is crucial for evaluating the quality of the DD test and the overall DEM calibration.

Table 2
Comparison between the experimental and DEM modelling results.

Parameters	Experiment	DEM Simulation		Deviation	
		ELB	SJKR	ELB	SJKR
Shear angle SA (deg)	66	67	58	+1.5 %	−12.1 %
Angle of repose AoR (deg)	38	33	40	−13.2 %	−5.3 %
Flow time (s)	1.2	1.1	1.7	−8.3 %	+41.2 %
Mass loss (%)	41.2	46.5	62.3	+5.3 %	+21.2 %
Average				**7.0 %**	**19.9 %**

5. Mass loss and new quantitative parameters to assess the drawdown test

5.1. New index to assess deformation characteristics of cohesive material in drawdown test

Previous sections proved that using conventional criteria such as the mass loss, AoR, SA and flow time to assess the performance of cohesive models in DD test is not always sufficient and reliable, because they do not include the influence of cohesion on the time-dependent response of the material. In this section a new assessment parameter called the Deformation Index (DI) is proposed to overcome this shortcoming. The DI is defined as the ratio between the vertical displacement of the material surface (H_L) and the initial height (H_0) of the fill material in the upper box. Fig. 6 shows how this index can be calculated and used to represent the material response with time. Furthermore, the influence of inter-particle cohesion can be reflected through the development of H_L, i.e., when particles become sticky with cohesive bonds their resistance to deformation induced by gravitational effect becomes larger.

Different types of cohesion such as different magnitudes and rupture conditions of the attractive force will directly affect the displacement H_L and the number of particles being discharged through the opening (the highlighted region in Fig. 6a). Fig. 6b shows how the DI varies significantly over cohesionless Hertz and cohesive SJKR and ELB models, depending on cohesive features and cohesive models. Note here that the best sets of parameters are used in this comparison. When particles are cohesionless (green curve), displacement develops immediately and reaches its maximum values ($DI = 1$). When the DI reaches its maximum value, displacement is equal to the initial height of the fill and a stable stage with slopes at two sides of the box is achieved. On the other hand, both cohesive models exhibited considerable delay (after 0.2–0.36 s) in rising displacement because the additional interparticle cohesion has retained a lot of particles and prevented them from migrating, thus preserving the original geometry of the system. Significant deformation only occurs when the equilibrium between forces of retention and gravity are broken and there is a subsequent fast growth of settlement. In fact, despite starting later, the DI by the ELB model developed faster (larger gradient) and reached its maximum level at the same time as the cohesionless model. The SJKR has a much larger delay time, and therefore, it reached the stable stage much later due to the larger interparticle attraction; this will be described later in this paper. Overall, these characteristics of DI are reasonable for experimental observations and can therefore be used to distinguish the behaviour of different cohesive contacts.

One interesting point is that although the ELB and SJKR resulted in different delay periods before triggering particle collapse, i.e., 0.2 and 0.36 s, their total duration from the beginning to the end of the discharging process was almost the same. Specifically, the ELB took 0.2 s to reach the stable stage, whereas this time was 0.24 s for the SJKR. Furthermore, Fig. 6c shows how the fill changed its shape with and without cohesion according to different stages. The cohesionless material has a symmetrical funnel shape with relatively flat slopes at both sides, whereas the cohesive materials have an irregular funnel shape with highly curved slopes at the first and second stages. In the final stage, the cohesive materials form trapezoid shaped slopes, not the convex slopes seen in the non-cohesive case. These contrasting responses between cohesive and non-cohesive materials due to the formation of particle clumps induced by inter-particle attraction will be explained in later sections. These numerical observations indicate that despite having

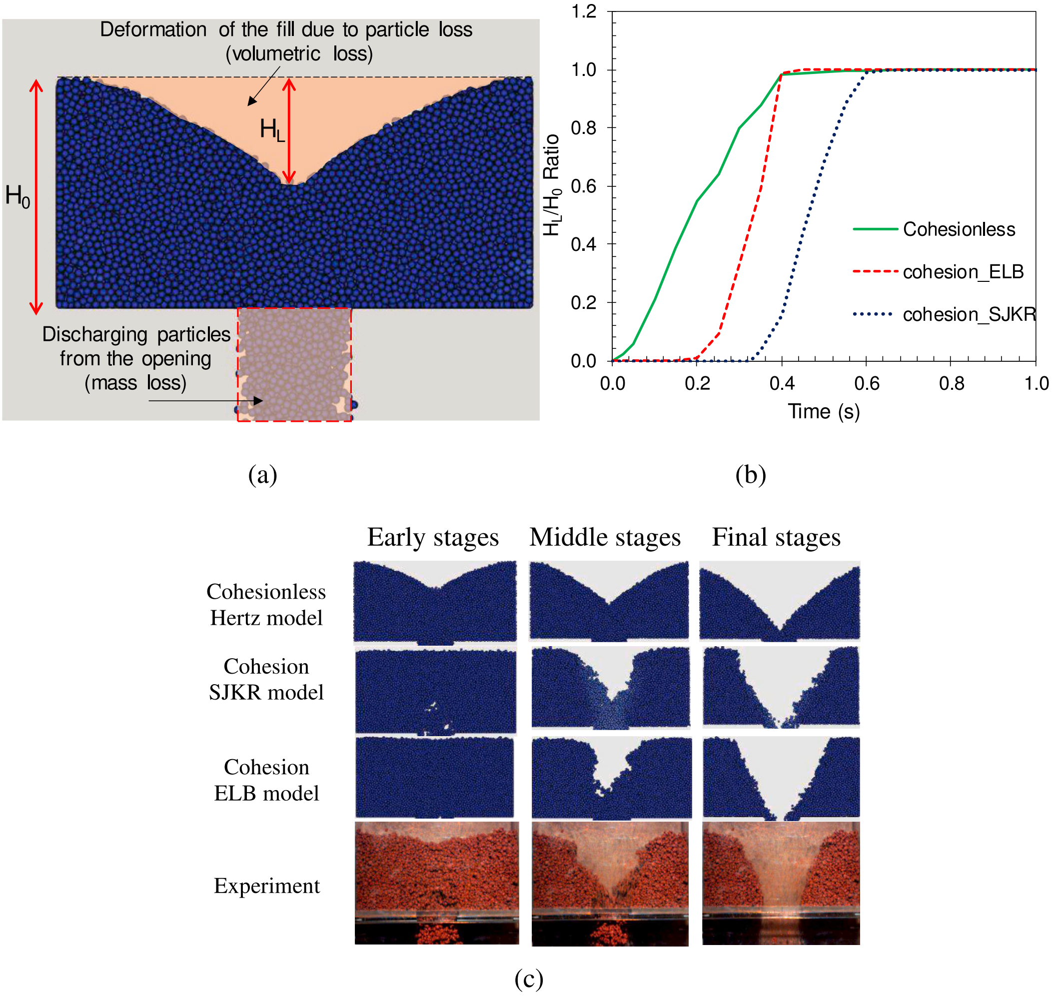

Fig. 6. Deformation behaviour of non-cohesive and cohesive materials in the DD test: (a) definition of deformation index DI, (b) variation of DI with time and (c) the formation of slopes in 3 different models in comparison with experimental observation.

the same DI value, the shape of the slopes (and thus the volumetric loss) and the mass loss of particles discharging from the upper box (highlighted region in Fig. 6a) can be very different. Furthermore, the proposed DI is only valuable when $H_L < H_0$ mainly within the first and second stages of DD test, while the response of material in later stage is not included. In this respect, the use of DI with other parameters such as the correlations between mass and volumetric losses to fully capture the influence of cohesion is necessary.

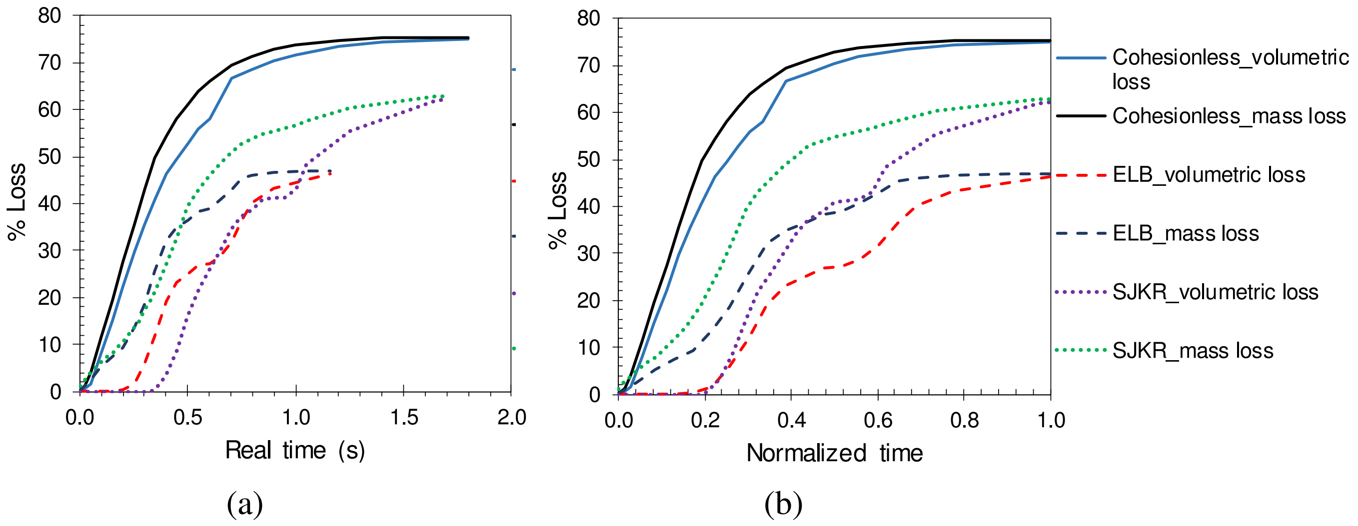

Fig. 7. Volumetric and mass losses recorded in (a) real time, and (b) normalized time.

5.2. Correlations between mass and volumetric losses of material in drawdown test

It is noteworthy that unlike cohesionless particles, cohesive particles can flow out of the upper box (i.e., the mass loss is the ratio of the total weight of particles that fell out of the upper box and the total weight of particles at the initial stage) at a certain degree without it having a significant impact on the shape (i.e., volumetric loss is ratio of the volume induced by the settlement of the upper material and total initial volume) of the fill (see Fig. 6a). This results in a deviation between the mass and volumetric losses of the material. For example, Fig. 7 shows that non-cohesive material has the largest mass and volumetric losses (up to 75 %) at the end of the test with their development curves that are almost identical in this case. In contrast, both cohesive cases resulted in much lower losses (i.e., 60 % and 43 % for SJKR and ELB, respectively) at the final stage and their volumetric and mass losses apparently deviated from each other. This indicates the key role of inter-particle cohesion in the response of mass and volumetric losses and why these variables need to be analysed over time in order to assess the performance of these models.

Fig. 8 shows the difference in the percentage loss of volume and mass over time as captured by different models. The data plots indicate that the largest deviation occurs in 0.42 s in all models. With the non-cohesive material, the maximum deviation was only 7.5 % whereas the percentages for the ELB and SJKR models are 13 % and 24 %, respectively. Notably, the SJKR model resulted in the highest peak which was in fact double that of the ELB outcome. This means that at a given time the number of particles retained by cohesion in the SJKR model is always higher than in the ELB model, and the higher the deviation the greater the ability to preserve the initial structure of particles. More importantly, the ELB model did not induce a specific peak, it maintained the largest value from 0.2 to 0.6 s (i.e., forming a plateau at 14 % loss). This indicates a more uniform flow of particles and a corresponding change in the volume of fill by the ELB model.

Comparing the proposed deformation index DI (Fig. 6) and the losses in mass and volume (Fig. 7 and Fig. 8), while the DI reaches its maximum value of 1 after around 0.6 s and remains constant until the end of the test, the mass and volumetric losses continue to increase until the final stage (1.8 s). Therefore, the correlation between DI and the mass and volumetric losses can be divided into 2 different stages. Initially, when the DI is actively increasing from 0 to 1 (0–0.6 s), during which the DI and the mass and volumetric losses linearly increase. However, in the second stage (> 0.6 s) where the DI becomes constant at 1 ($H_L = H_o$), there is no specific correlation between these parameters. This means that the proposed DI is valuable during initial stage where particles are highly dynamic under drawdown process that the mass and volumetric losses cannot present accurately the deformation of material. In contrast, the mass and volumetric losses are mainly referred in later stage.

Fig. 9 shows variation in the bulk density of material in the upper box over time. The bulk density (i.e., ratio between mass and bulk volume of material) represents how much the fill volume changes per unit loss of mass. In this analysis, the bulk density was estimated by measuring the mass and volume of material remaining in the upper box in DEM simulation over time. The results show that this bulk density immediately dropped significantly across different cases. For the cohesionless case, the density decreased from approximately 1450 to around 1200 kg/m^3 after 0.6 s before sharply rising back, which means that after 0.6 s the mass loss balances the volumetric loss. Unlike cohesionless material, this ratio did not increase immediately after reaching the bottom, it in fact fluctuated for a while before gradually rising back to the original level for both ELB and SJKR models. This result indicates that cohesion has prolonged the duration that particles can be retained in the upper region before beginning to collapse under the loss of particles at the opening. Interestingly, the density by the ELB took only 1.15 s to get back to the initial value, whereas it took 1.75 s for SJKR model. More importantly, the density by the SJKR dropped substantially to only around 1050 kg/m^3, but this change was much smaller in the ELB case (1240 kg/m^3). This means that the material modelled by SJKR retained its volume much more compared to that by the ELB, given the same amount of mass loss in the upper box. This is consistent with earlier observations (e.g., Fig. 6). Despite variation in magnitude, the results presented over normalized time (Fig. 9b) show almost identical patterns between the two cohesive models, thus indicating a consistent influence of inter-particle cohesion on the deformation behaviour of the fill.

6. Microscale evolution of the drawdown test while considering the effect of cohesion

6.1. Contact behaviour and the formation of shear angle in the upper box

How the attractive force develops and breaks with the relative displacement between particles can significantly affect the total and average contact numbers in the system and in individual regions. The average contact number (n_{ca}) per particle was computed to assess the response of material during a DD test at particle scale. Fig. 10 shows how the n_{ca} changed in the entire system over time, as captured by different models. It shows there are three different stages in the evolution of the contact number during a DD test. In the first stage, the n_{ca} decreased with time in each case because the particles began to move out of the

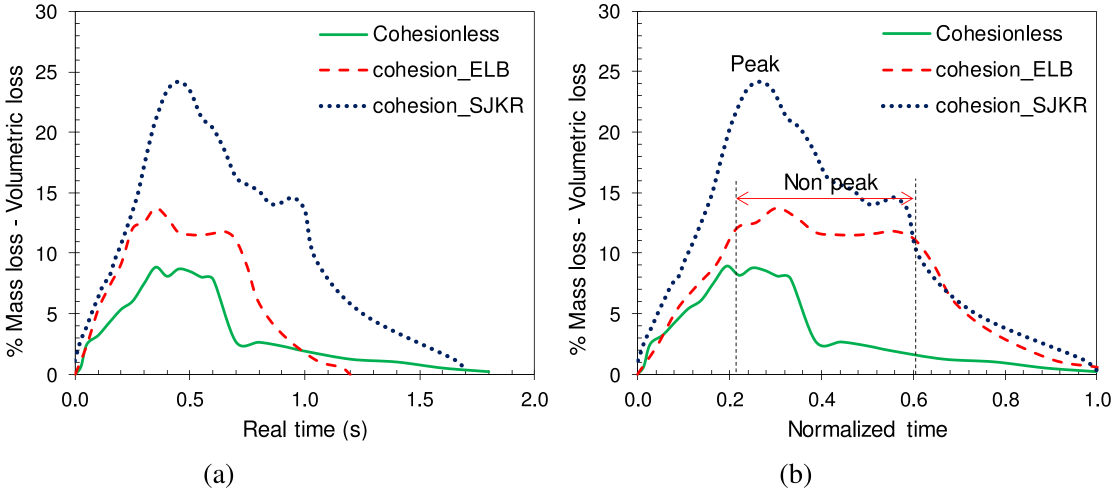

Fig. 8. Difference in the mass and volumetric losses of the upper fill in (a) real time, and (b) normalized time.

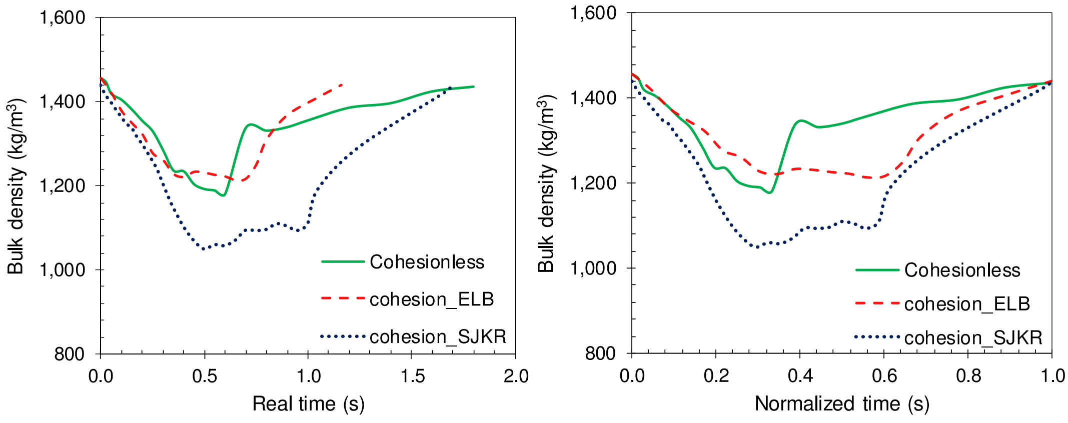

(a) (b)

Fig. 9. Changes in the bulk density of material in the upper box with time: (a) real time, and (b) normalized time.

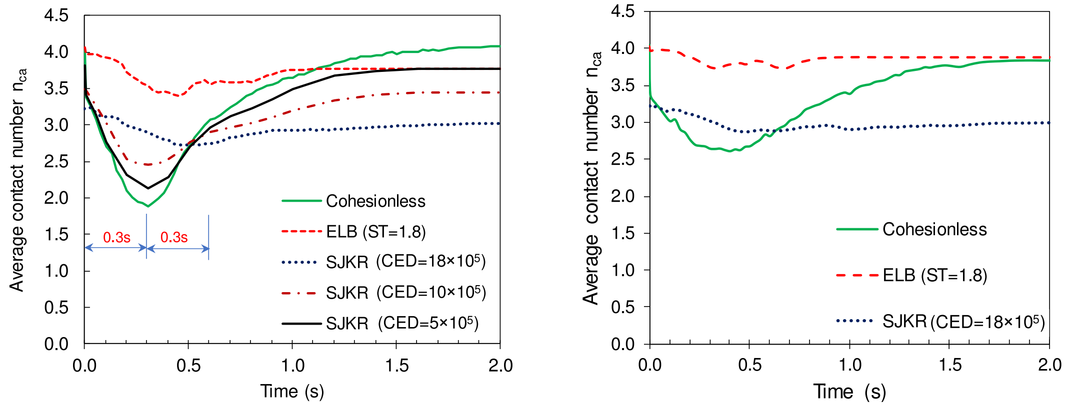

(a) the entire system (b) the upper box

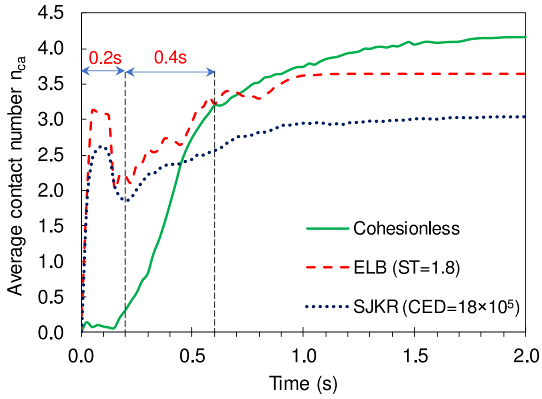

(c) the lower box

Fig. 10. The average contact number with time for (a) the entire system by all models during 2 s, (c) the upper box, and (d) the lower box.

upper box, thus lowering the number of dropped contacts. In the second stage, the n_{ca} rose back after reaching its lowest level at around 0.3–0.4 s. During this stage the particles in the lower box accumulated to a significant level that was enough to compensate for the loss of particle contact in the upper box, thus the total n_{ca} increases. In the final stage, the n_{ca} becomes stable mostly after 1.5 s. Fig. 10 also indicates the different and varying magnitudes of n_{ca} depending on the cohesion coefficients and cohesive models. Generally, with an increasing cohesive force the fluctuation amplitude of the n_{ca} decreased considerably. For instance, the n_{ca} amplitude changed within the range of 1.9–4.1 for cohesionless, but it decreased to between 2.5 and 3.3 when CED $= 10 \times 10^5$ J/m^3; furthermore, it narrowed to 2.7–3.2 when the CED increased to 18×10^5 J/m^3. In the ELB case the n_{ca} ranged from 3.4 to 4.1 at the highest surface tension of ST $= 1.8$ N/m.

The above results also show large differences in the number of contacts between non-cohesive and cohesive materials, especially during the 1st and 2nd stages. For example, in the entire system (Fig. 10a) and the upper box (Fig. 10b), the n_{ca} of cohesionless particles dropped sharply and reached the bottom first whereas in cohesive cases the n_{ca} gradually decreased and developed later. Fig. 10a shows that the n_{ca} of non-cohesive particles decreased quickly to 1.9 at approximately 0.3 s, but the n_{ca} of cohesive materials decreased to around 2.5 for the SJKR model and 3.4 for the ELB model. For highly cohesive materials such as ST $= 1.8$ N/m and CED $= 18 \times 10^5$ J/m^3 it took about 0.5 s for the n_{ca} to reach the lowest magnitude. This was understandable because the cohesive particles remained their contact bonds in the form of large clumps while falling out the upper box (see Fig. 11b) and that prevented the n_{ca} from decreasing. On the other hand, particles without cohesion (Fig. 11a) tended to become looser with minimal contact when falling, and thus the smallest n_{ca} was at the 1st stage.

The opposite behaviour of non-cohesive and cohesive particles can also be seen in the lower box (Fig. 10). While the n_{ca} of non-cohesive particles was very small (almost zero) during the initial stage (i.e., 0.15 s), it developed rapidly and reached its peak (2.5–3) during this time. The reason for this can be attributed to the falling particles which tend to spread out widely (minimal contact with each other) after hitting the lower box, but nevertheless, they still continue together as large clusters under inter-particle cohesion to form a larger n_{ca} at the early stage. It is also interesting to see that for cohesive materials the n_{ca} fluctuated after reaching the bottom, for example, at 0.2 s, the value of n_{ca} decreased and then recovered (Fig. 10). This phenomenon occurred because when clumps of particles fell and hit the lower box they broke into smaller clumps, resulting in a certain decrease in the number of contacts. The n_{ca} recovered when the accumulated clumps of particles became larger as new contacts formed. Compared to the SJKR, the ELB resulted in larger n_{ca} in both the upper and lower boxes; the reason for this phenomenon will be discussed in later sections.

Similar to the contact number, the contact force was also assessed to enhance our understanding of the DD test at particle scale. Fig. 12 summarizes the average contact force per particle in the entire system for the upper and lower box. For the whole system and the upper box, cohesion significantly enhances the particle to particle contact force. For instance, at the initial stages the contact force of the SJKR model (1.05 N) is around 10 times greater than the cohesionless particles (0.10 N), whereas this ratio is only 2.5 times for the ELB model (0.25 N). This indicates that using the SJKR model with a large CED to obtain the best fit for shape features with the experimental results can result in unreasonable contact forces between particles. When comparing the contact force by the best models of SJKR and ELB, the contact force by the SJKR model is 4 times larger than the ELB model. In theory, the key difference between these 2 models is that the SJKR simplified the calculation of attractive force by directly multiplying the CED with the contact area as represented in Eq. (7), whereas the ELB model is totally independent of the contact area. This means that the attractive force from the ELB model does not change abruptly due to the quick movement and large overlap of particles, unlike the SJKR. Furthermore, this difference arises from the fact that the cohesive force component of the SJKR model only exists when particles overlap each other and then vanishes when there is no overlap. In contrast, the cohesive force in the ELB model can still be active even when two particles are away from each other, as shown in Fig. 1 and Fig. 2.

It is of interest to note that in the lower box the difference between non-cohesive and cohesive cases is insignificant during the initial stage and only increases after 0.15 s. This occurs because in the first 0.15 s the particles fell and were dispersed widely, resulting in limited contacts and interaction forces at the early stage. The inclusion of inter-particle cohesion causes a rise in the contact force; for instance, the largest contact force increased from 0.06 N for non-cohesive materials to 0.08 N for cohesive materials, whereas with cohesive particles the contact forces increased rapidly and dropped sharply; they also continued to fluctuate apparently over time.

6.2. *Porous structure and the formation of angle of repose in the lower box*

6.2.1. *Pattern of contact network*

In order to understand how falling particles can arrange their structure while forming an angle of repose (AoR) in the lower box, an assessment of the particle contact network across the bottom section of the material piles was carried out. The same thickness, i.e., the largest diameter D_{max} was considered across 3 different models. The cross sections in (Fig. 13) showed that interparticle cohesion induced attractive forces between particles that formed chain-like connections and promoted a heterogeneous porous structure, resulting in a larger porosity. For instance, the cohesionless cross section exhibited a more uniform distribution of particles and pores (marked by red circles), whereas the

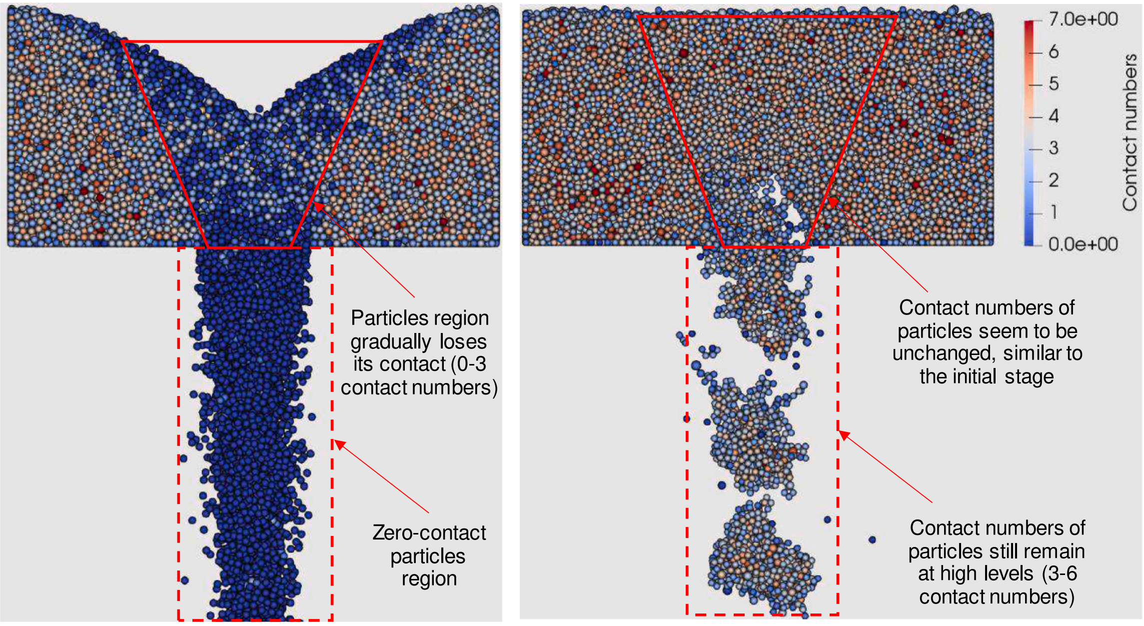

(a) cohesionless (b) cohesion

Fig. 11. Observation of falling particles (a) cohesionless, and (b) cohesive.

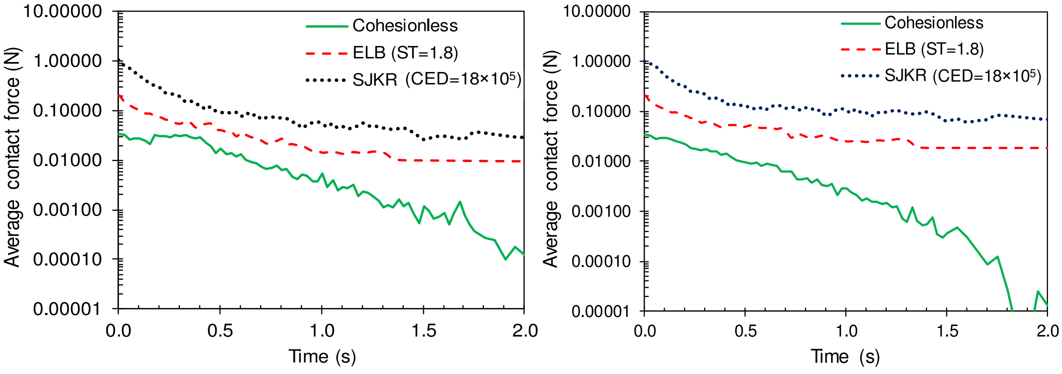

(a) The entire system

(b) The upper box

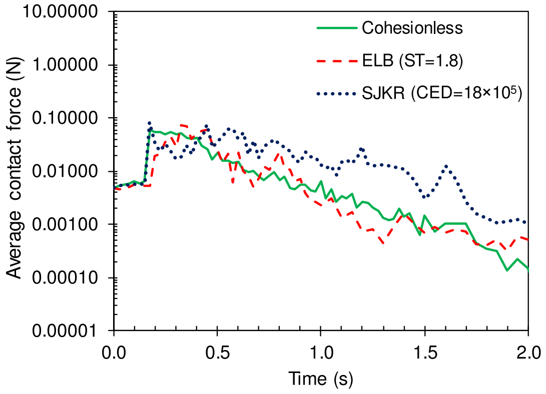

(c) The lower box

Fig. 12. Variation of the average contact force over time for (a) the entire system, (b) the upper box, and (c) the lower box.

generation of chain-like connections (highlighted by yellow rectangles) in cohesive media facilitated larger pores (yellow circles). This observation of a chain-like microstructure in cohesive systems corroborates previous studies [51,52], where cohesion was found to form a more heterogeneous porous structure in particulate media. The larger voids observed in the current DEM models may correspond to a phenomenon namely increasing open microfabrics structure due to cohesion, as described in previous experiments involving mixtures of sand and clay [53,54]. However, no previous studies have investigated the underlying mechanism of this phenomenon based on the different cohesive concepts addressed in this current study.

One noteworthy observation in Fig. 13 is that large voids only form when surrounding the chain-like structures, whereas small voids only exist when the chain-like structures are absent. This strongly suggests that the generation of chain-like structures is the major reason for the formation of large and heterogeneous pores. Fig. 13 b and c also highlight the difference in microstructure between the 2 cohesive models (SJKR and ELB). The ELB model does not form localised blocks (highlighted in Yellow), the particles and voids are distributed more uniformly with a minimal chain-like structure. As a contrast, the SJKR model exhibits widespread chain-like elements (highlighted in Yellow) that result in a greater percentage of large voids.

The distributions of pore size at the base of material pile in the lower box at stable (final) stage are shown in Fig. 14. In this analysis, an image processing was applied on 2D plan view of particles at the bottom layer to estimate the pore size. This technique has been applied effectively to capture porous features of porous media in previous studies, further details can be found in [55,56]. To minimize boundary effect, a region in the middle (190 × 168 mm) was selected for the calculation. Although there is a certain difference between the pore size in 2D and 3D, the current analysis is useful to understand how cohesion can influence on the pore size distribution of granular material. To better highlight the difference in pore size among different cases, the pore sizes in all simulations were normalized with the size of the largest pore in the SJKR case. The results show that the pore sizes in cohesionless medium are significantly smaller and distributed more uniform compared to cohesive particles. The SJKR model resulted in larger pore size with wider range compared to the ELB model.

6.2.2. *Contact number and stabilisation conditions*

To quantify the influence of chain-like connections on the morphology of the contact network, we explored the distributions of contact numbers in non-cohesive and cohesive systems. Fig. 15a and b show how frequently different contact numbers are encountered in the system when there are varying degrees of cohesion in the SJKR and ELB models, respectively. The distribution of contact numbers for the cohesionless system are relatively right-skewed with the highest frequency (nearly 30 %) between 3 and 4 contacts and with a wider distribution to the right (> 4). This agrees with previous investigations into the stability of particulate systems under gravity [8,52], where an average of 3 to 4 contacts per particle was found to be the optimum condition needed to faciliate stabilisation. However, increasing inter-particle cohesion makes the distribution more uniform such that the peak of frequency migrates to the left (i.e., 2–3 contacts/particle). The larger the conhesion, the larger the percentage of structures owning smaller contact number. In fact, almost 45 % of the number of contacts ≤ 2 indicates predominance of chain-like connections in the particulate structure. Nevertheless, with the inclusion of cohesion the contact strength increased significantly and enhanced the structural stability enough to sustain the same AoR with fewer inter-particle contacts.

The above simulations demonstrated that the SJKR and ELB models were characterised by a large difference in the distribution of contact

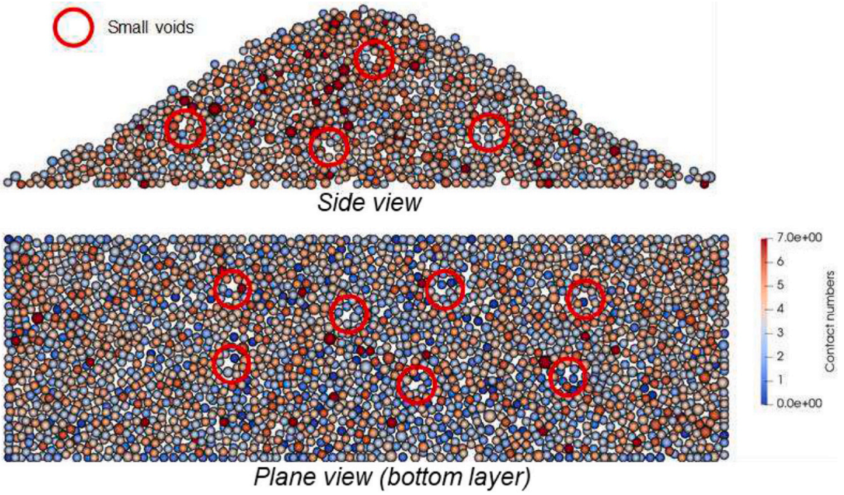

a) Cohesionless

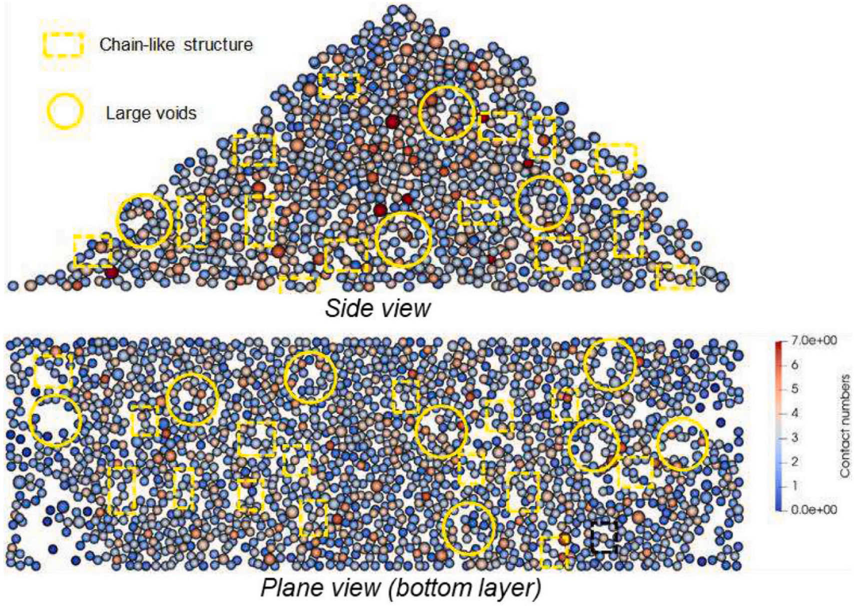

b) Cohesion (SJKR CED=18×10^5 J/m^3)

Fig. 13. Observation of the cross-sections of non-cohesive and cohesive particles forming AoR in the lower box: (a) cohesionless Hertz model (b) SJKR model, and (c) ELB model.

numbers. They exhibited the ultimate level at which the frequency-contact number curves approach with increasing cohesion, whereby the most predominant number of contacts at the ultimate level by the ELB model was 3.1, which was larger than the corresponding contact number 2.3 by the SJKR model (see Fig. 15c). This explains why the ELB model resulted in more uniform porous sytems and fewer chain-like connections. An increasing cohesion will result in a larger attractive force between particles, but this does not mean this is the highest stability a particulate structure can have. Past investigations [55,56] into the influence of micro-fabric on the shear strength of soil indicates that the more uniform the contact network and the finer distribution of pores that a soil can have, the better the resistance to external loading such as compression and cyclic excitation. The key criterion needed to determine a robust and uniform porous system from this current study is that the largest average number of contacts should be higher than 3 to eliminate the chain-like structure.

Fig. 16 compares the peak average contact number (n_{peak}) that varies with the different degrees of cohesion predicted by the SJKR and ELB models. For the SJKR model, when the cohesion coefficient CED increased constantly from zero to 18 × 10^5 J/m^3, n_{peak} decreased continuously from 3.5 to 2.3 (see Fig. 16a). For the ELB model however, n_{peak} only decreased from 3.5 to approximately 3.1 when the surface tension ST rose from zero to 0.75 (N/m). When the ST further increased from 0.75 to 1.8 N/m there was no significant change in the value of n_{peak}, in fact, it became stable around 3.05 despite the ST increasing further (see in Fig. 16b). This suggests that there is an intriguing relationship between the peak average contact number (n_{peak}) and the formation of AoR such that when the n_{peak} exceeded 3 the AoR tended to be less than 35 (see Fig. 16c); this indicates that the higher the contact number the lower the porosity. Conversely, when the n_{peak} was less than 3 the AoR surpassed 35 with a greater percentage of chain-like structures and larger pores. This observation underscores the critical role of the

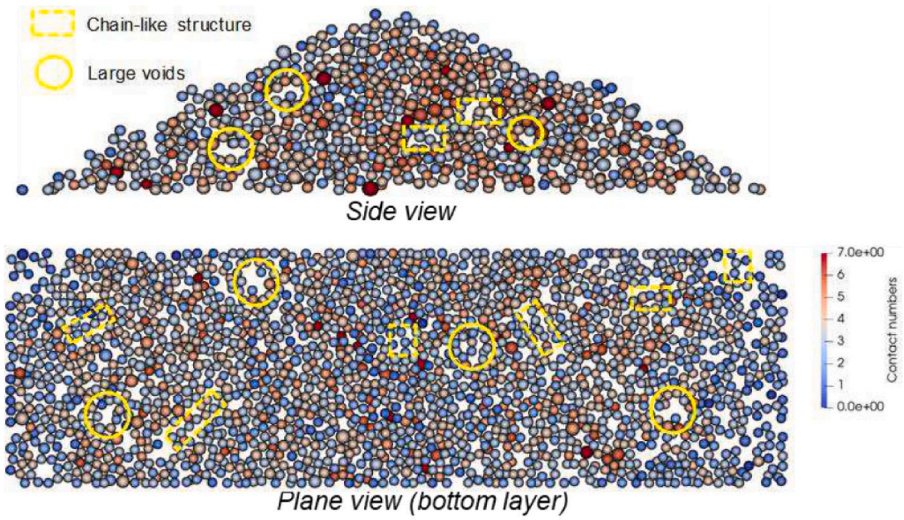

c) Cohesion (ELB ST=1.8 N/m)

Fig. 13. (*continued*).

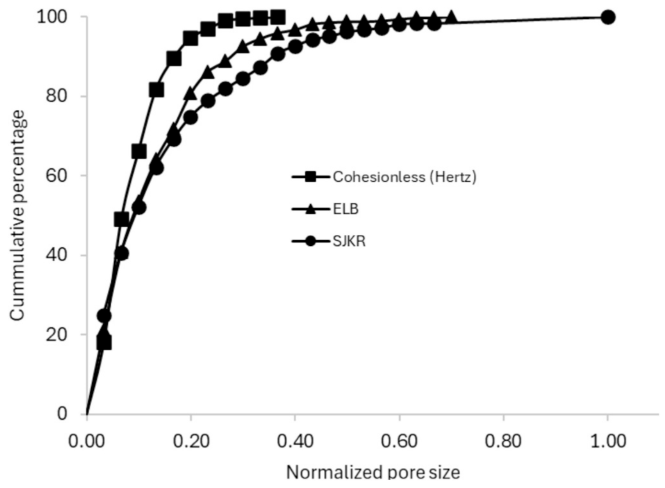

Fig. 14. Distribution of pore size at the base (2D) of material pile (cone) in the lower box (stable stage) simulated by Hertz (cohesionless), ELB and SJKR models.

peak average contact number in determining the formation of a chain-like structure.

6.2.3. *Contact forces*

In order to further understand the intrinsic mechanism that governs the contact behaviour of particles in the SJKR and ELB models, the contact area, the tangential force, torque, and normal force of cohesive systems were normalized with values from the cohesionless systems. These results (Fig. 17) show the large changes in the contact area and the corresponding tangential force, torque, and normal force when cohesion increased. While both the models generally agree that increasing the cohesion coefficients (CED and ST) will enlarge the contact area, they also provide different rates by which the contact area can increase. For example, when the CED developed from 0 to under 7.5×10^5 (J/m^3) in the SJKR model the contact area grew by a slope of 3.0, but then it swiftly increased by a slope of 8.75 when the CED $> 7.5 \times 10^5$ (J/m^3). On the other hand, the ELB showed an opposite response whereby the contact area increased faster during the early stage and then slowed down at the end. Specifically, when the ST increased from zero to 0.75 N/m the contact area increased by a factor of 1.2, but when the ST $>$ 0.75 N/m the growth rate apparently decreased. The contact area in the SJKR model was more sensitive to increasing the coefficient of cohesion because it increased faster and reached a larger magnitude (i.e., 2 times larger at the end). The same responses can also be seen for the normal and tangential forces, and torque arising around the contact area. This behaviour is understandable when referring to Eq. (7), where the attractive force in the SJKR model was compuated based on the contact area A and CED. It is important to note that the attractive force is only distributed inside the contact area and is derived from the internal overlap. The larger the attractive force induced by increasing the CED (see Fig. 12), the larger the contact area needed to maintain the system in equilibrium. Furthermore, Fig. 17a shows that when the contact area increases significantly, the corresponding normal and tangential forces, and the torque, also increased accordingly.

The above observations point to an important threshold whereby further increasing the cohesion coefficient will result in a substantial change in the response of the contact area. For instance, when the CED exceeded 7.5×10^5 J/m^3 in the SJKR model it generated a large attractive force between particles, thereby increasing the contact area substantially; in fact, the rate of increment apparently changed from 3.0 to 8.75 before and after this milestone. On the contrary, for the ELB model, the contact area increased faster when ST $<$ 0.75 (N/m) (Fig. 17b). There was less dependence by the contact area on the cohesion coefficient in the ELB model, as its governing equation shows (Eq. (8)). Unlike the SJKR model, the attractive force is distributed outside the contact area according to Eq. (10), so when the coefficient of cohesion increased the corresponding rise in suction force did not significantly affect the size of the contact area. As a result there was less influence from rising cohesion on the normal forces, tangential forces, and torque, which are heavily derived from the contact area (Fig. 17b).

7. Practical implications of the interparticle cohesive SJKR and ELB models

7.1. *Relationship between interparticle cohesion and macroscale quantities*

It is important to understand the connection between microscale parameters such as interparticle cohesion and macroscale quantities such as the AoR and shear angle (SA) in the DD test. Fig. 18 shows quantitative relationships between the cohesive coefficients (CED and ST) and the AoR and SA, where the predictive accuracy of the proposed

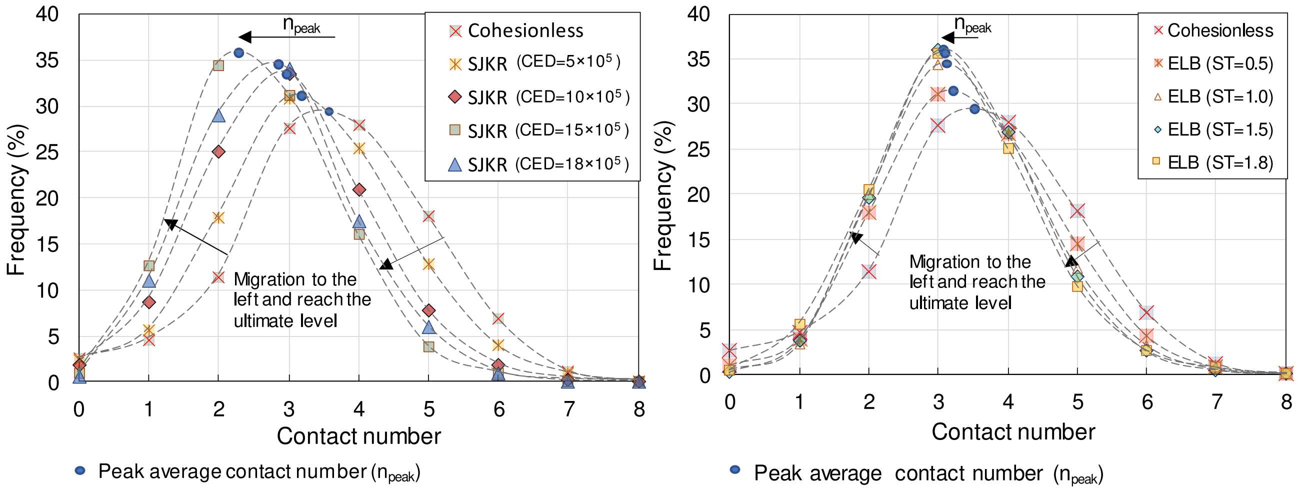

(a) SJKR model (b) ELB model

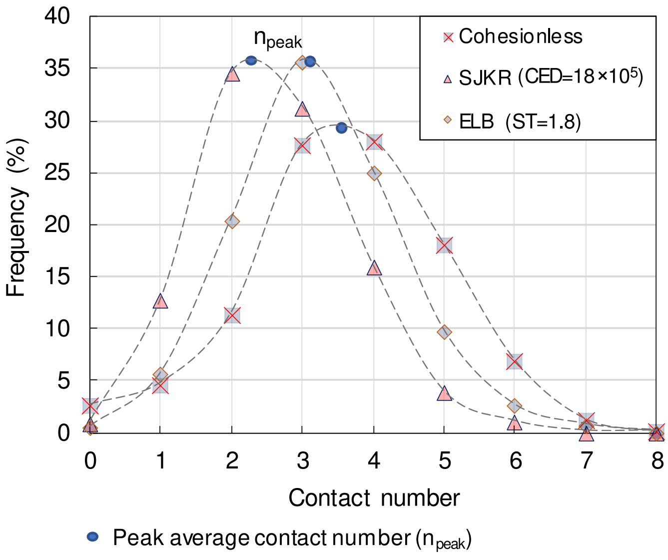

(c) For best predictions by SJKR and ELB models.

Fig. 15. Distribution of contact numbers for (a) SJKR model, (b) ELB model and (c) comparison between the SJKR and ELB models for the best predictions. **Note**: dashed splines connecting individual points aim to represent the shift in the contact distribution, they do not represent real contact numbers of particles.

empirical equations can reach a very high degree ($R^2 > 0.98$). For the SJKR model, the linear correlations between the CED and macro-parameters (AoR and SA) are shown in Fig. 18a (i.e., $R^2 > 0.99$), whereas the opposite responses of AoR and SA to the varying ST in the ELB model is shown in Fig. 18b. Specifically, when the ST increased, the SA also increased linearly to high degree (60–70^0), but the AoR only increased slightly at the early stage before decreasing to become constant at the same level as that in the cohesionless case (ST = 0). In other words, the AoR predicted by the ELB model remained almost unchanged and was much smaller than that estimated by the SJKR approach, albeit subjected to constantly increasing cohesion in both models. In this regard, the ELB model showed more reasonable outcomes, because wet particles tend to have weak bonds and friction (lubricating effect), especially under a dynamic impact and when falling from a certain height (upper box); there is also a smaller angle of repose. On the other hand, when the cohesion increased in the upper box (static state), the larger tensile strength in particle bonding increased the resistance of the material to collapse under effect of gravity, thus leading to more remaining particles and a higher SA (Fig. 18a). This response of SA to varying cohesion was consistent in the SJKR and ELB models.

Fig. 19 shows the variations in the porosity with the degree of cohesion and the relationship between the porosity and the peak average contact number. In this analysis, the bottom layer (see Fig. 13) of the cone (AoR) built inside the lower box was considered. The results showed that the porosity by the SJKR model increased constantly and reached 0.67 when the CED increased from zero to 18 × 10^5 J/m^3. On the other hand, the porosity by the ELB model only increased to 0.5 at ST = 1.0 N/m and then stabilised at this level despite the ST continuing to increase to 1.8 N/m. This response is very relevant to the behaviour of particle contacts and microstructure that have been described earlier. The SJKR model resulted in predominant chain-like contacts that formed large and non-uniform pores, as shown in Fig. 13b, whereas the

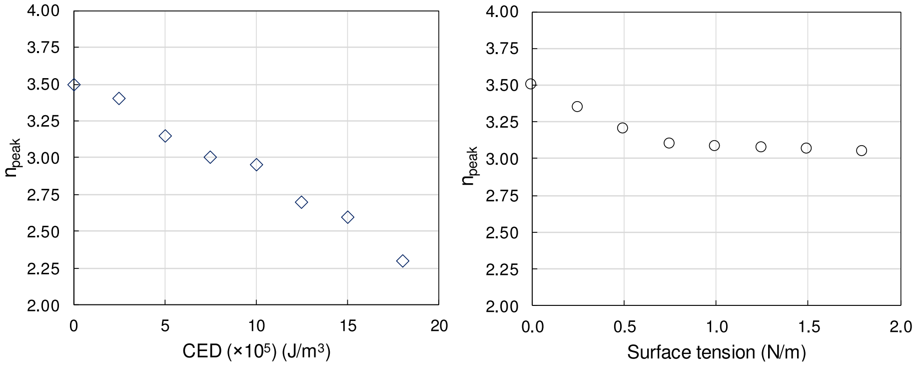

a) SJKR model

(b) ELB model

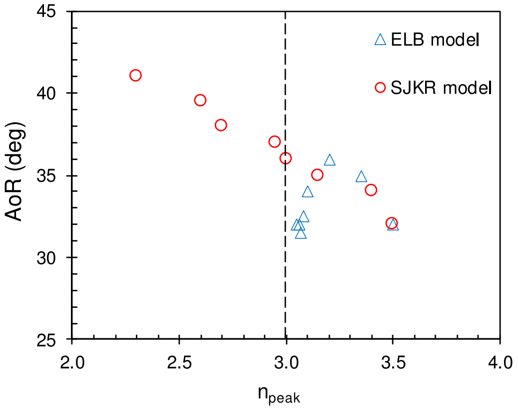

(c) Influence of n_{peak} on the AoR

Fig. 16. The peak average contact number against the cohesion degree by (a) the SJKR model, (b) the ELB model, and (c) the influence on the AoR (combined two models).

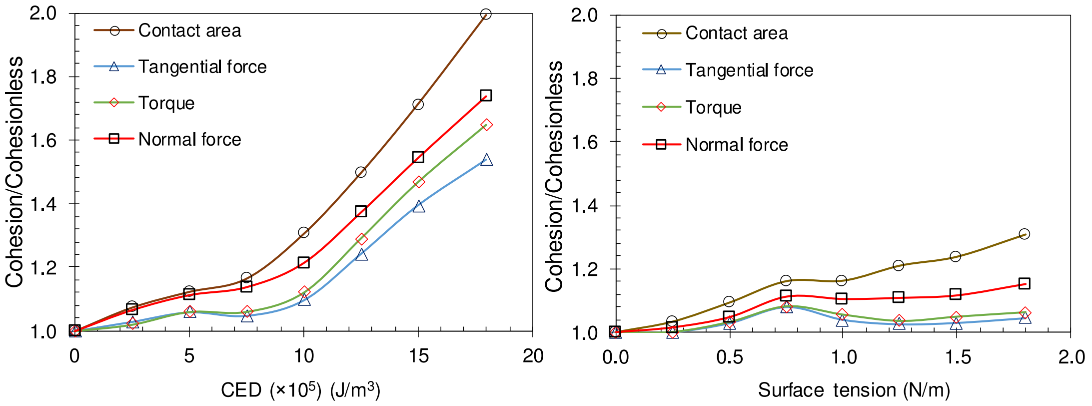

(a) SJKR model

(b) ELB model

Fig. 17. The influence of varying cohesion on the contact area, tangential force, torque, and normal force of the (a) SJKR model, and (b) the ELB model.

ELB model produced closed and more uniform pores. By examining the results of the 2 models, we find that Fig. 19c shows a linear relationship between the porosity and the peak average contact number ($R^2 = 0.94$). For granular materials such as sand, a porosity from 0.45 to 0.55 (corresponding to the peak average contact number $n_{peak} \geq 3$) can be considered as medium compaction, whereas above this range ($n_{peak} < 3$) there is a loose and weak condition. This specific finding proves that there is a unique relationship between the porosity and the contact number that can be used in practice to define the stability criterion for granular soils.

7.2. Implications to modelling of wet cohesive granules

It is not uncommon in DEM simulations that a wet state of particles could be generated by activating cohesive models from dry conditions [18–20,23]; this can lead to a large impact on the initial geometric and structural conditions of specimens. Despite this, no previous study given this serious consideration, for example, Fig. 20 shows how the contact number and volume of the granular medium change when interparticle cohesion was added by two different models. While the SJKR causes a significant influence on the initial condition of the specimen, the ELB did

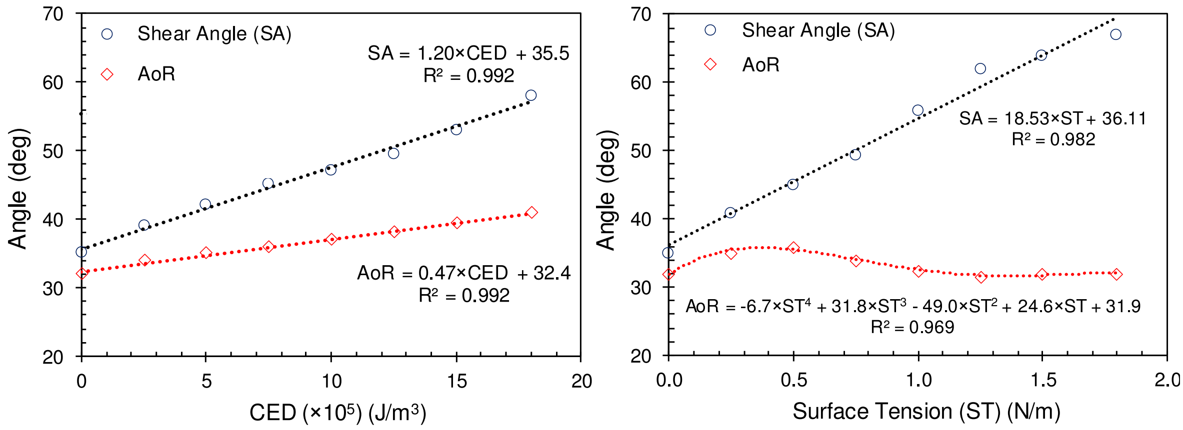

(a) SJKR model (b) ELB model

Fig. 18. Relationship between macro-parameters (AoR and SA) and interparticle cohesion coefficients (CED and ST) in the (a) SJKR model, and (b) the ELB model.

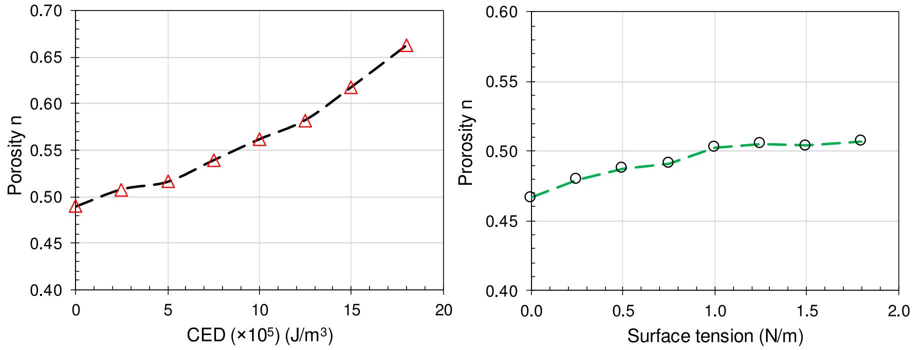

(a) SJKR model (b) ELB model

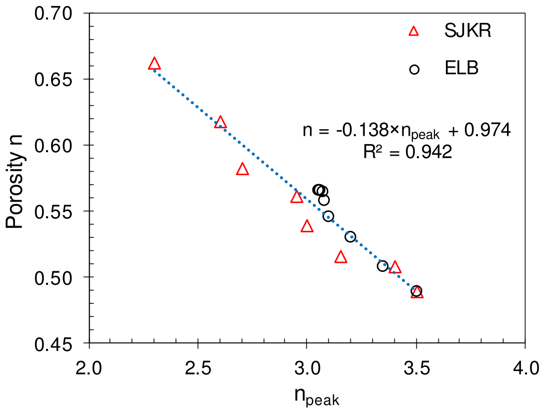

(c) the peak average contact number

Fig. 19. Variation of porosity in the lower box with the degree of cohesion for the (a) SJKR mode; (b) the ELB model, and (c) the peak average contact number.

not, despite having the same constant rise in their degree of cohesion. Specifically, when the CED increased to 18 × 10^5 J/m^3, the contact number by the SJKR declined from 4.0 to 3.2, while the volume increased by almost 7 % (see Fig. 20a). This occurred because the very high attractive force between particles under an increasing CED tended to promote the chain-like pattern that reformed porous structure with larger porosity as explained earlier (Fig. *13* and Fig. *16*). Despite having the same mass, different cohesive models induced different potential energies that can be stored within the interparticle bonds and depends on the cohesive component at the contact points. This affected not only the initial condition of the test samples, but also their dynamic responses including both micro- and macroscopic features as discussed earlier. In this regard the ELB which had a marginal impact on the initial condition of the specimens becomes much more relevant to granular contexts. It is interesting to note that despite having the same.

Considering the extensive investigations into various macro- and micro-aspects of simulating DD tests using the SJKR and ELB models above, it can be concluded that the use of SJKR model for wet granules exhibits considerable limitations that could significantly influence the predicted outcomes. A CED > 10 × 10^5 J/m^3 can result in a large distortion of particulate fabric with an increasing chain-like structure that becomes irrelevant to most granular materials such as wet sand and mining wastes. Even though there can be a good agreement between experiment and modelling for the macro-features such as the AoR and

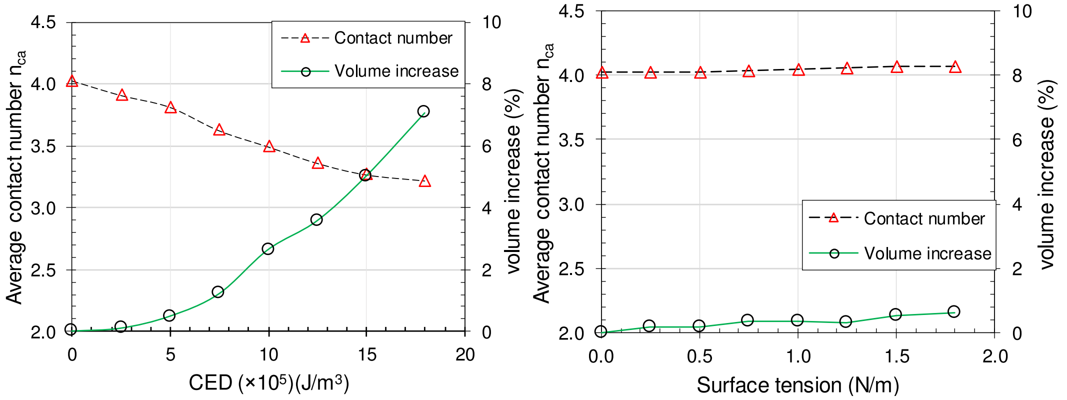

Fig. 20. Influence of cohesion on the contact numbers and volume of the initial state of specimens in (a) SJKR model and (b) the ELB model.

shear angle, the time-dependent response and microscale characteristics would seriously deviate from the realistic behaviour of materials. It is noteworthy that although previous studies have attempted to model wet granules by adopting the DD test for calibration, they often focussed on several visible aspects such as the shape features while ignoring many crucial features such as the time-dependent response and the micro-scale behaviour of particles. This oversight can lead to inappropriate judgement and the use of cohesive models that fail to predict accurately and comprehensively the behaviour of wet materials. On the other hand, the ELB model based on the true tension and breakage of a liquid bridge at the contact rather than simplification through a single cohesion parameter, i.e., the CED in the SJKR was found to be highly relevant at simulating wet granules.

8. Conclusions

This study provided a novel and comprehensive assessment against the modelling effectiveness of cohesive materials in DEM by adopting two distinct cohesive models, namely the simplified JKR (SJKR) and Easo Liquid Bridge (ELB) for wet granules through the drawdown (DD) test. Apart from macro-features such as the shear angle (SA) and angle of repose (AoR) which were often addressed in previous studies, the current work described micro-scale quantities such as particle interaction and porous structure that defined the intrinsic mechanism underpinning the material response. New time-dependent parameters that capture the deformation response and volume-mass change correlations were developed to improve our understanding of material behaviour in the DD test. Through this process the performance of two cohesive models were assessed, giving valuable implications to the future modelling of cohesive materials. The salient outcomes of this study lead to the following conclusions:

- The ELB model outperformed the SJKR when considering 4 macro-aspects, i.e., the SA, AoR, flow time, and mass loss. Compared to the experimental data, the average predictive error for these 4 parameters by the ELB model was only 7 %, which was almost one third of that produced by the SJKR model. The shear angle SA predicted by the ELB model only deviated by 1.5 % from the experimental value, whereas in the SJKR model it was 12.1 %. This brings to the conclusion that the ELB model is effective in modelling different configurations in the intrinsic behaviour of liquid-induced cohesive granular materials.
- Newly proposed assessment parameters such as the Deformation Index (DI) and the correlations (the difference and ratio) between volumetric and mass losses proved to be rigorous and comprehensive enough to evaluate the performance of modelling against the time-dependent response of cohesive materials. For example, the DI, which changed significantly with cohesion, only began to develop after 0.2 s when the cohesion coefficient ST = 1.8 N/m. The difference between the volumetric and mass losses were good enough to characterize different cohesion-independent responses, for instance, its peak value increased from 7.5 % in cohesionless cases to 13 % and 24 % for cohesive cases using the ELB and SJKR models.
- The particle-scale investigation led to a conclusion that using only macro-shape features such as the SA and AoR to validate cohesive modelling was insufficient. The SJKR and ELB models could successfully reproduce the shape of collapsing slopes at the final stage, but they had totally different characteristics in time-dependent variables, particle contact, and porous structure that required appropriate attention. For example, the SJKR took approximately 41 % longer to reach a stable state, whereas it was only 8.1 % for the ELB model. In a practical sense, these outcomes undoubtedly imply that both calibration and validation of modelling cohesive granules must be implemented with rigorous consideration of time-dependent and microscale behaviours.
- With the SJKR model, when CED $> 10 \times 10^5$ J/m^3, this high attractive force promoted the formation of chain-like structures that decreased the peak average contact number (n_{peak}) to less than 3, resulting in an increasing porosity and distorted porous structure. On the other hand, the ELB model maintained a stable porosity with unchanged n_{peak} (approximately 3.1) when its cohesion coefficient ST increased and exceeded 1 N/m. In this regard, one may conclude that the ELB model is able to generate a more uniform porous structure, and thereby prevent the material model from attaining an unstable state.
- The shear angle (SA) (in the upper box) was found as a linear function of cohesion, i.e., the larger the cohesion the larger the shear angles. The SA could reach maximum values of 60^0 and 70^0 at the largest degree of cohesion. On the other hand, the angle of repose (in the lower box) AoR reached 41^0 when predicted by the SJKR model at CED = 18×10^5 (J/m^3); however, it stabilised at 36^0 and then decreased slightly as the cohesion coefficient ST increased (nonlinear relationship) in the ELB model. This result leads to the conclusion that the ELB model can deliver more realistic outcomes when modelling wet granules in drawdown testing, compared to other DEM models considered in this study.

Despite the above successes, significant efforts are still required to develop highly accurate experiment of drawdown test where the time-dependent and microscale responses of material can be obtained in detail. The results from this test will enable a complete validation of DEM modelling, giving valuable data to develop more fundamental concepts as well as validating governing parameters of cohesive contact models.

CRediT authorship contribution statement

Thien Q. Huynh: Writing – original draft, Validation, Software, Methodology, Investigation, Formal analysis, Conceptualization. **Thanh T. Nguyen:** Writing – review & editing, Supervision, Resources, Project administration, Methodology, Investigation, Funding acquisition, Formal analysis, Conceptualization. **Buddhima Indraratna:** Writing – review & editing, Supervision, Project administration, Conceptualization.

Declaration of competing interest

The authors declare the following financial interests/personal relationships which may be considered as potential competing interests:

Thanh T. Nguyen reports financial support was provided by Australian Research Council. If there are other authors, they declare that they have no known competing financial interests or personal relationships that could have appeared to influence the work reported in this paper.

Acknowledgements

This study was supported by Australian Research Council (DE230101127) and Transport Research Centre (TRC), University of Technology Sydney.

Data availability

The data used in the current study are available from the corresponding author upon reasonable request.

References

[1] J. Chen, A. Anandarajah, Van der Waals attraction between spherical particles, Journal of Colloid, Interface Sci. (1996) 519–523.

[2] F. Soulie, F. Cherblanc, M.S. El Youssoufi, C. Saix, Influence of liquid bridges on the mechanical behaviour of polydisperse granular materials, Int. J. Numer. Anal. Methods Geomech. (2006) 213–228.

[3] R. Schwarze, A. Gladkyy, F. Uhlig, S. Luding, Rheology of weakly wetted granular materials: a comparison of experimental and numerical data, Granul. Matter 15 (2013) 455–465.

[4] S. Roy, A. Singh, S. Luding, T. Weinhart, Micro–macro transition and simplified contact models for wet granular materials, Comput. Part. Mech. 3 (2016) 449–462.

[5] C. O'Sullivan, J.D. Bray, M.F. Riemer, Influence of particle shape and surface friction variability on response of rod-shaped particulate media, J. Eng. Mech. 128 (2002) 1182–1192.

[6] C. Wensrich, A. Katterfeld, Rolling friction as a technique for modelling particle shape in DEM, Powder Technol. 217 (2012) 409–417.

[7] W. Chen, T. Donohue, K. Williams, A. Katterfeld, T. Roessler, Modelling cohesion and adhesion of wet sticky iron ores in discrete element modelling for material handling processes, in: Proceedings of the Iron Ore Conference, Perth, Australia, 2019, pp. 13–15.

[8] T. Doan, B. Indraratna, T.T. Nguyen, C. Rujikiatkamjorn, Coupled CFD-DEM modelling of clogging of granular columns by cohesive fines, Comput. Geotech. 177 (2025) 106902.

[9] S. Matsusaka, H. Maruyama, T. Matsuyama, M. Ghadiri, Triboelectric charging of powders: A review, Chem. Eng. Sci. 65 (2010) 5781–5807.

[10] Y.I. Rabinovich, M.S. Esayanur, B.M. Moudgil, Capillary forces between two spheres with a fixed volume liquid bridge: theory and experiment, Langmuir 21 (2005) 10992–10997.

[11] K.L. Johnson, K. Kendall, A. Roberts, Surface energy and the contact of elastic solids, Proc. R. Soc. Lond. A 324 (1971) 301–313.

[12] S.M. Derakhshani, D.L. Schott, G. Lodewijks, Micro–macro properties of quartz sand: Experimental investigation and DEM simulation, Powder Technol. 269 (2015) 127–138.

[13] T.T. Nguyen, B. Indraratna, A coupled CFD–DEM approach to examine the hydraulic critical state of soil under increasing hydraulic gradient, Int. J. Geomech. 20 (2020) 04020138.

[14] M.J. Carr, T. Roessler, P.W. Robinson, H. Otto, C. Richter, A. Katterfeld, C. A. Wheeler, Calibration procedure of Discrete Element Method (DEM) parameters for wet and sticky bulk materials, Powder Technol. 429 (2023) 118919.

[15] H.-G. Matuttis, A. Schinner, Particle simulation of cohesive granular materials, Int. J. Modern Phys. 12 (2001) 1011–1021.

[16] S. Luding, Cohesive, frictional powders: contact models for tension, Granul. Matter 10 (2008) 235–246.

[17] F. Gilabert, J.-N. Roux, A. Castellanos, Computer simulation of model cohesive powders: Influence of assembling procedure and contact laws on low consolidation states, Phys. Rev. E 75 (2007) 011303.

[18] A.P. Grima, Quantifying and modelling mechanisms of flow in cohesionless and cohesive granular materials, Doctor of Philosophy thesis, in: School of Mechanical, Materials & Mechatronic Engineering, University of Wollongong, 2011.

[19] M. Ajmal, T. Roessler, C. Richter, A. Katterfeld, Calibration of cohesive DEM parameters under rapid flow conditions and low consolidation stresses, Powder Technol. 374 (2020) 22–32.

[20] T. Roessler, C. Richter, A. Katterfeld, F. Will, Development of a standard calibration procedure for the DEM parameters of cohesionless bulk materials–part I: Solving the problem of ambiguous parameter combinations, Powder Technol. 343 (2019) 803–812.

[21] C. Coetzee, O.C. Scheffler, Comparing particle shape representations and contact models for DEM simulation of bulk cohesive behaviour, Comput. Geotech. 159 (2023) 105449.

[22] C. Hoshishima, S. Ohsaki, H. Nakamura, S. Watano, Parameter calibration of discrete element method modelling for cohesive and non-spherical particles of powder, Powder Technol. 386 (2021) 199–208.

[23] T. Doan, B. Indraratna, T. Nguyen, C. Rujikiatkamjorn, Influence of microscale cohesive contacts on the macro-behaviour of soils through DEM investigation, in: Smart Geotechnics for Smart Societies, CRC Press, 2023, pp. 229–243.

[24] M.J. Mohajeri, C. van Rhee, D.L. Schott, Replicating cohesive and stress-history-dependent behavior of bulk solids: Feasibility and definiteness in DEM calibration procedure, Adv. Powder Technol. 32 (2021) 1532–1548.

[25] W. Chen, A. Roberts, A. Katterfeld, C. Wheeler, Modelling the stability of iron ore bulk cargoes during marine transport, Powder Technol. 326 (2018) 255–264.

[26] M.J. Carr, T. Roessler, P.W. Robinson, H. Otto, C. Richter, A. Katterfeld, C. A. Wheeler, Calibration procedure of Discrete Element Method (DEM) parameters for wet and sticky bulk materials, Powder Technol. 429 (2023) 118919.

[27] C. Kloss, C. Goniva, LIGGGHTS–open source discrete element simulations of granular materials based on Lammps, in: Supplemental Proceedings: Materials Fabrication, Properties, Characterization, Modeling 2, 2011, pp. 781–788.

[28] S.C. Thakur, J.P. Morrissey, J. Sun, J. Chen, J.Y. Ooi, Micromechanical analysis of cohesive granular materials using the discrete element method with an adhesive elasto-plastic contact model, Granul. Matter 16 (2014) 383–400.

[29] C. Ramírez-Aragón, J. Ordieres-Meré, F. Alba-Elías, A. González-Marcos, Comparison of cohesive models in EDEM and LIGGGHTS for simulating powder compaction, Materials 11 (2018) 2341.

[30] Q.T. Phan, H.H. Bui, G.D. Nguyen, A. Bouazza, Effect of particle rolling resistance on drained and undrained behaviour of silty sand, Acta Geotech. (2021) 1–26.

[31] N.H.T. Nguyen, T.T. Nguyen, Q.T. Phan, Dynamics and runout distance of saturated particle-fluid mixture flow on a horizontal plane: A coupled VOF-DEM study, Powder Technol. 408 (2022) 117759.

[32] LIGGGHTS, LIGGGHTS(R)-PUBLIC Documentation, Version 3.X, 2023.

[33] C. O'Sullivan, Particulate Discrete Element Modelling: A Geomechanics Perspective, Spon Press (an imprint of Taylor & Francis), London, 2011.

[34] E.J. Parteli, J. Schmidt, C. Blümel, K.-E. Wirth, W. Peukert, T. Pöschel, Attractive particle interaction forces and packing density of fine glass powders, Sci. Rep. 4 (2014) 6227.

[35] J. Chen, D. Krengel, D. Nishiura, M. Furuichi, H.-G. Matuttis, A force–displacement relation based on the JKR theory for DEM simulations of adhesive particles, Powder Technol. 427 (2023) 118742.

[36] M. Ucgul, J.M. Fielke, C. Saunders, Three-dimensional discrete element modelling of tillage: Determination of a suitable contact model and parameters for a cohesionless soil, Biosyst. Eng. 121 (2014) 105–117.

[37] D. Newitt, A contribution to the theory and practice of granulation, Trans. Inst. Chem. Eng. 36 (1958) 422–442.

[38] G. Lian, C. Thornton, M.J. Adams, A theoretical study of the liquid bridge forces between two rigid spherical bodies, J. Colloid Interface Sci. 161 (1993) 138–147.

[39] C.D. Willett, M.J. Adams, S.A. Johnson, J.P. Seville, Capillary bridges between two spherical bodies, Langmuir 16 (2000) 9396–9405.

[40] L.A. Easo, C. Wassgren, Comparison of liquid bridge volume models in DEM simulations, in: 2013 AIChE Annual Meeting, 2013.

[41] S.T. Nase, W.L. Vargas, A.A. Abatan, J. McCarthy, Discrete characterization tools for cohesive granular material, Powder Technol. 116 (2001) 214–223.

[42] F. Gabrieli, R. Artoni, A. Santomaso, S. Cola, Discrete particle simulations and experiments on the collapse of wet granular columns, Phys. Fluids 25 (2013).

[43] T. Doan, B. Indraratna, T.T. Nguyen, C. Rujikiatkamjorn, Interactive role of rolling friction and cohesion on the angle of repose through a microscale assessment, Int. J. Geomech. 23 (2023) 04022250.

[44] J. Pachón-Morales, H. Do, J. Colin, F. Puel, P. Perré, D. Schott, DEM modelling for flow of cohesive lignocellulosic biomass powders: Model calibration using bulk tests, Adv. Powder Technol. 30 (2019) 732–750.

[45] K. Iwashita, M. Oda, Rolling resistance at contacts in simulation of shear band development by DEM, J. Eng. Mech. 124 (1998) 285–292.

[46] J. Ai, J.-F. Chen, J.M. Rotter, J.Y. Ooi, Assessment of rolling resistance models in discrete element simulations, Powder Technol. 206 (2011) 269–282.

[47] T. Roessler, A. Katterfeld, DEM parameter calibration of cohesive bulk materials using a simple angle of repose test, Particuology 45 (2019) 105–115.

[48] Y. Feng, D. Owen, Discrete element modelling of large scale particle systems—I: exact scaling laws, Comput. Part. Mech. 1 (2014) 159–168.

[49] Y. Liu, H. Liu, H. Mao, The influence of rolling resistance on the stress-dilatancy and fabric anisotropy of granular materials, Granul. Matter 20 (2018) 1–16.

[50] M.A. Behjani, N. Rahmanian, A. Hassanpour, An investigation on process of seeded granulation in a continuous drum granulator using DEM, Adv. Powder Technol. 28 (2017) 2456–2464.
[51] P. Rognon, J.-N. Roux, D. Wolf, M. Naaïm, F. Chevoir, Rheophysics of cohesive granular materials, Europhys. Lett. 74 (2006) 644.
[52] J. Xu, R. Zou, A. Yu, Analysis of the packing structure of wet spheres by Voronoi–Delaunay tessellation, Granul. Matter 9 (2007) 455–463.
[53] I.B. Gratchev, K. Sassa, V.I. Osipov, V.N. Sokolov, The liquefaction of clayey soils under cyclic loading, Eng. Geol. 86 (2006) 70–84.
[54] M. Goudarzy, D. Sarkar, W. Lieske, T. Wichtmann, Influence of plastic fines content on the liquefaction susceptibility of sands: monotonic loading, Acta Geotech. (2022) 1–19.
[55] T.T. Nguyen, B. Indraratna, Micro-CT scanning to examine soil clogging behavior of natural fiber drains, J. Geotech. Geoenviron. 145 (2019) 04019037.
[56] I.N. Silva, B. Indraratna, T.T. Nguyen, C. Rujikiatkamjorn, The influence of soil fabric on the monotonic and cyclic shear behaviour of consolidated and compacted specimens, Can. Geotech. J. 61 (2024).